catalysts

MDPI

Article

Structural Engineering of SAPO-34/ZSM-5 Core–Shell Zeolites for Regulating Shape Selectivity and Surface Acidity in Molybdenum-Catalyzed Methane Dehydroaromatization

Charitomeni M. Veziri *, Aggeliki Papavasiliou, George V. Theodorakopoulos, Fotios K. Katsaros and George E. Romanos *

National Center for Scientific Research "Demokritos", Institute of Nanoscience and Nanotechnology, Agia Paraskevi, 15341 Athens, Greece; a.papavasiliou@inn.demokritos.gr (A.P.); g.theodorakopoulos@inn.demokritos.gr (G.V.T.); f.katsaros@inn.demokritos.gr (F.K.K.)
* Correspondence: c.vezyri@inn.demokritos.gr (C.M.V.); g.romanos@inn.demokritos.gr (G.E.R.)

Abstract

In this study, novel Mo-decorated core–shell zeolite composites, namely ZSM-5@SAPO-34 and SAPO-34@ZSM-5, were synthesized and evaluated as catalysts for methane dehydroaromatization (MDA). Core–shell structures were effectively fabricated via sequential hydrothermal synthesis, utilizing SAPO-34 and ZSM-5 as cores, which were subsequently subjected to hydrothermal growth in ZSM-5 and SAPO-34 reacting solution, respectively. Catalysts with varying SAPO-34/ZSM-5 mass ratios and Mo loadings were thoroughly characterized by the XRD, BET, SEM-EDS, and NH_3-TPD techniques. The catalytic performance in the MDA reaction revealed a strong correlation between composite architecture, acidity, Mo dispersion, and product selectivity. Introducing H^+SAPO-34 into both core–shell composites enhanced ethylene-to-benzene conversion due to the acidic confinement provided by SAPO-34. In contrast, non-protonated SAPO-34@ZSM-5 showed limited activity as a result of its weak acidity and inadequate Mo dispersion. Among all catalysts, H^+ZSM-5@SAPO-34 with a 3:1 core–shell mass ratio delivered the highest benzene yield and stability, outperforming the benchmark, H^+ZSM-5. This work highlights the potential of tailored core–shell zeolite composites in optimizing acid–metal interactions and improving catalytic performance in hydrocarbon transformations.

Keywords: SAPO-34; ZSM-5; core–shell zeolites; protonation; Bronsted acidity; molybdenum species; MDA

Academic Editor: Antonia Iazzetti

Received: 12 December 2025
Revised: 16 January 2026
Accepted: 20 January 2026
Published: 3 February 2026

1. Introduction

The fundamental processes for conversion of methane into value-added chemicals are conducted via either an indirect route with the interference of syngas production or by the direct transformation of methane into aromatics in the absence of oxygen, which takes place in a single step, thus saving energy and reducing costs. The most prominent non-oxidative process, which has gained significant attention over recent years, is methane dehydroaromatization (MDA) via oligomerization of methane to benzene and hydrogen [1]. Mo-decorated zeolites have been identified as the most active catalysts for MDA [2]. The H^+ZSM-5 zeolite in particular is considered a multi-functional catalyst, offering the advantages of Brønsted acidity, pore shape selectivity, and enhanced surface area platform for Mo dispersion [3]. The prevailing mechanism involves the activation of methane over molybdenum species, serving as the reaction's rate-limiting step, ultimately resulting in the

formation of CHx species through dehydrogenation [4]. These species subsequently form ethylene, which is further subjected to oligomerization and cyclization, resulting in the formation of higher hydrocarbons and aromatics on the Brønsted acid sites of the H^+ZSM-5 substrate [5]. However, a notable drawback of the Mo/ZSM-5 catalyst is the substantial accumulation of carbonaceous deposits, impeding its catalytic efficiency [6]. Given the strong interest in Mo/HZSM-5 catalysts, an extensive number of studies have reported on improvements in converting methane to desired aromatics. In this direction, the main focus has centered on controlling the chemical nature and location of Mo species. Li et al. prepared a Mo/ZSM-5 catalyst and achieved a well-dispersed species, both inside the zeolitic channels and at the external surface of the zeolite [7]. They found that Mo-oxicarbide species originated from internal Mo-oxide particles, serving as the primary catalytic active centers with the longest catalyst lifespan during the reaction. In contrast, Mo-carbide species, arising from Mo-oxide aggregates at the external surface of the zeolite, were swiftly deactivated. Liu et al. conducted a thorough investigation of the interactions occurring between H^+ZSM-5 and SiO_2 catalyst supports with Mo species in the MDA reaction. They observed that, in the first case, MoO_x interacted with Brønsted acid sites, whereas the interactions of MoO_x with SiO_2 were comparatively weaker [8]. They also deduced that Mo-oxide species linked to Brønsted acid sites exhibited higher catalytic activity and an extended operational lifespan compared to Mo-oxide species deposited on a non-acidic support. Volmer et al. explored various molybdenum precursors and different loading conditions in an attempt to enhance Mo dispersion. They demonstrated that achieving an adequate benzene yield was only possible when Mo was attached as a cationic mono- or dimeric species. Conversely, catalyst activity was hindered when MoO_3 aggregates formed at the external surface of the zeolite, coinciding with an increase in coke formation [9]. Kosinov et al. demonstrated a significant correlation between framework stability and Mo loading during high-temperature calcination and oxidative regeneration [10]. Their findings revealed that at low Mo loading, Mo species were situated in zeolite micropores as cationic mono- and dinuclear Mo-oxo complexes, maintaining stability even at increased calcination temperatures. However, with higher Mo loading, a structural transformation occurred, converting Mo species from isolated Mo-oxo entities to Mo-oxide aggregates primarily located on the external surface of the zeolite. The migration of these species into the zeolitic framework required temperatures exceeding 550 °C, leading to the destabilization of the MFI framework.

Shape selectivity is the key property which established medium-pore zeolites such as ZSM-5, which are suitable for MDA reaction, as their pore size and shape are expected to increase benzene selectivity. On the other hand, small-pore zeolites have gained significant attention due to the exhibition of high selectivity values towards light hydrocarbons. Small-pore and cage-like SAPO-34, for instance, is a well-known shape-selective catalyst towards light olefins in the methanol-to-olefin (MTO) reaction, since ethylene and propylene are the only products, and can escape from the small pore apertures. Medium-pore ZSM-5, however, falls behind in the production of light olefins due to its reduced pore space compared to SAPO, despite being effective in generating a significant amount of aromatics [11]. Among the SAPO family, SAPO-34 not only surpasses all other topologies in small-olefin production, but also outperforms the similarly structured SAPO-44 and SSZ-13, indicating that beyond shape selectivity, surface reactivity is a key factor in enhancing catalytic activity [12,13]. The main assets that render SAPO-34 an ideal option for MTO, aside from pore architecture and acid strength, include the particle size and Si content, which can be easily controlled by manipulating the reacting solution and synthesis conditions. Since ethylene is an intermediate product in the MDA reaction, Mo-supported SAPO-34 could be a potential candidate. Few studies have been reported on Mo-supported small-pore zeolites

for MDA reactions. Mo/SAPO-34 and Mo/H-SSZ-13, both of which have CHA topology, have exhibited methan conversion one order of magnitude lower than Mo-supported medium-pore H^+ZSM-5. This is mainly attributed to the formation of carbon deposits, as benzene molecules cannot escape from small CHA pore apertures [13]. Similarly, the benzene selectivity of Mo/SAPO34 was much lower (73%) compared to 91% for Mo/ZSM5. No conversion to aromatics, on the other hand, was obtained on Mo/H-SSZ-13, indicating that the surface reactivity of the catalyst support can determine the mechanism of reaction.

The synthesis of integrated zeolite structures has advanced significantly in recent years, enabling the engineering of pore architectures and active sites through the synergy of different pore geometries and surface properties, as well as the emergent behavior of the resulting composites [14,15]. Exploitation of different combinations of framework types with various proportions, crystal sizes, and core/shell configurations of the zeolite substituents has offered a tuning of the catalytic properties of the composite structures, such as shape/size selectivity and surface reactivity, towards specific applications, together with a longer catalyst lifetime [16–20]. Core–shell structures consisting of SAPO-34 and ZSM-5 are the most studied composite zeolites for olefin production, as is the case with their parent components [21]. ZSM-5, as the core, is the most frequent type of composite since it is more tolerant to exposure to SAPO-34 reacting solution. SAPO-34, on the contrary, is diluted in the strong basic environment of ZSM-5 and needs a pretreatment step to enhance its stability. Li et al. synthesized SAPO34@ZSM5 by employing functionalized SAPO-34 as the core. The composite exhibited improved ethylene and propylene yield in ethanol transformation compared to parent SAPO due to the induced core–shell characteristics [17]. In another study conducted by Chen et al., a core–shell structure was achieved by introducing a ZSM-5 core into the reaction mixture of SAPO. The overgrown composite outperformed the physical mixture of the components in olefin production during MTO. When laponite was used as the SAPO silicon source, Li and Mg metals were introduced into the zeolitic framework, enhancing olefin selectivity and catalyst stability [22]. Wu et al. successfully fabricated a SAPO-34@ZSM-5 composite that achieved a light olefin selectivity of 92.7% by mixing the two precursor solutions that had undergone a thermal pre-crystallization treatment. The excellent catalytic performance was attributed to the optimized acidity of the composite and the hierarchical mesoporous structure generated by the etching of SAPO-34 [23]. Another reaction that has been studied lately on ZSM5@SAPO34 core–shell structure is methanol to aromatics. Although SAPO-34 showed low selectivity towards aromatics due to its limited acidity and narrow porosity, the core–shell configuration with a double proportion of ZSM5 over SAPO surpassed the selectivity of the parent ZSM-5. This improvement is mainly attributed to the hierarchy and modest acidity of the composite [24]. Zhang et al. reported similar results by introducing ZSM-5 into the SAPO-34 synthesis gel containing a mesoporous agent. Increasing the ZSM-5 content adjusted the acidity in a way that promoted aromatic formation. Moreover, the hierarchical structure of the resulting composite created additional reaction pathways, allowing it to surpass even acidic ZSM-5 in aromatic selectivity [25]. Few investigations have explored the application of core/shell structures in the MDA reaction. Jin et al. synthesized an H^+ZSM-5/Silicalite-1 core–shell structure and successfully tuned the acidity of H^+ZSM-5 by controlling the amount of Silicalite-1 grown on the zeolite. Although the composite catalyst showed an overall decrease in acidity, and thus a reduced capacity to anchor molybdenum species, it exhibited strong shape selectivity, retained sufficient acidity, and demonstrated lower coke formation [26]. In a recent study, Hong et al. employed a reverse core–shell zeolite structure consisting of a silicalite-1 core and a ZSM-5 shell for MDA. By tuning both crystal size and aluminum content, the authors achieved a controlled spatial distribution of Al atoms, specifically, a reduction in aluminum on the external surface, which proved bene-

ficial in suppressing coke formation. However, the formation of silanol (Si–OH) groups compromised the activity of the Mo species, limiting the overall catalytic performance [27].

In the present study, we managed to obtain ZSM5@SAPO34 and SAPO-34@ZSM-5 core–shell structures by introducing core crystals (SAPO-34 and ZSM-5) into the reacting solution for the formation of the shell structure (ZSM-5 and SAPO-34), respectively. Functionalization of SAPO-34 with tetrapropylammonium bromide (TPABr) produced a dual effect: TPA^+ helped maintain the SAPO-34 structure against phase transformation and also served as a template for the growth of a ZSM-5 shell over SAPO-34. To introduce additional acid sites, the Na^+ ions in ZSM-5@SAPO-34 were exchanged with ammonium ions. Molybdenum species were then dispersed on both ZSM-5@SAPO-34 and SAPO-34@ZSM-5 by wet impregnation with ammonium heptamolybdate, and the resulting catalysts were evaluated in the MDA reaction. To the best of our knowledge, this is the first time that Mo has been incorporated into a core/shell zeolite composite to study the MDA reaction. Composites with different mass ratios of the two components, i.e., SAPO-34 and ZSM-5, and molybdenum of various loadings were tested for aromatic formation to corroborate the combined effect of SAPO content and core/shell conformation on the evolved acidity, which ultimately determined the dispersion and speciation of Mo species. Physicochemical properties of the various core/shell conformations and the respective ones upon loading with molybdenum were characterized by X-ray diffraction (XRD), Nitrogen 77K adsorption isotherms, an electron microscope with an energy-dispersive X-ray spectrometer (SEM-EDS), and temperature-programmed desorption of ammonia (NH_3-TPD).

2. Results and Discussion

2.1. Physicochemical Characterization of Parent Zeolites and Core/Shell Structures

2.1.1. Structure and Morphology of SAPO-34@ZSM-5, H^+[SAPO-34@ZSM-5], Mo(x)_SAPO-34@ZSM-5 and Mo(x)_H^+[SAPO-34@ZSM-5] Core/Shell Configurations Synthesized by One-Step Crystallization

The SAPO-34@ZSM-5 core–shell configuration was initially synthesized by directly introducing SAPO-34 crystals into the ZSM-5 synthesis solution following a pre-crystallization step. Although the resulting composite displayed characteristic diffraction peaks corresponding to both ZSM-5 (2θ = 7.9°, 23.1°, 23.9°, 24.4°) and SAPO-34 (2θ = 9.5°, 12.9°, 20.7°, 30.8°), the microporous framework of SAPO-34 was not preserved and collapsed into a dense $AlPO_4$–cristobalite phase after calcination. SEM images and XRD patterns of the SAPO-34@ZSM-5 composites before and after SAPO-34 framework destabilization are provided in the added Supplementary Material (Figure S1) [28,29].

SAPO-34@ZSM-5 core/shell structures were subsequently synthesized by functionalizing SAPO-34 with TPABr. TPA^+ served a dual role as a nucleation site, guiding the growth of ZSM-5 over SAPO and preserving the SAPO framework from dissolution in the strong basic environment of the ZSM-5 reacting mixture. Figure 1 displays the SEM images of SAPO-34@ZSM-5 with varying proportions of constituent zeolites in the resulting composites. By measuring the weight before and after the shell growth process, we achieved ZSM-5 loadings on SAPO-34 of 50% and 75% (Figure 1a,b). Mo loadings of 1, 3, and 6 wt% were deliberately selected to represent low, intermediate, and high metal contents, a strategy commonly employed in methane dehydroaromatization studies to assess the influence of Mo loading on metal dispersion, speciation, and catalytic performance. This range enables evaluation of the transition from highly dispersed MoO_x species at low loadings to less desirable aggregated Mo phases at higher loadings. Moreover, the chosen loadings allow systematic investigation of Mo contents below and above the critical ~4 wt% threshold [30]. The SEM image of Figure 1c corresponds to the SAPO-34@ZSM-5_75% composite upon loading with 6 wt% Mo. The apparent defects on the surface of SAPO

are indicative of the interactions between Mo species and support. The XRD patterns of the corresponding composites upon loading with molybdenum (Figure 1d) contain the main characteristic peaks of SAPO-34 and ZSM-5, demonstrating the role of TPABr as a protecting factor of SAPO-34 structural integrity during synthesis. Meanwhile, the high dispersion of Mo species on the surface and/or in the channels of the untreated composites for both high and low Mo loadings was confirmed, as the patterns showed no evidence of MoO_3 crystallite formation. What is intriguing is the more pronounced reduction in crystallinity observed in the composite with the greater amount of SAPO at a low Mo content. This may suggest that lower Mo loadings enhance the migration of MoO_x species in the micropores of SAPO, leading to a more pronounced effect on the zeolite crystallinity.

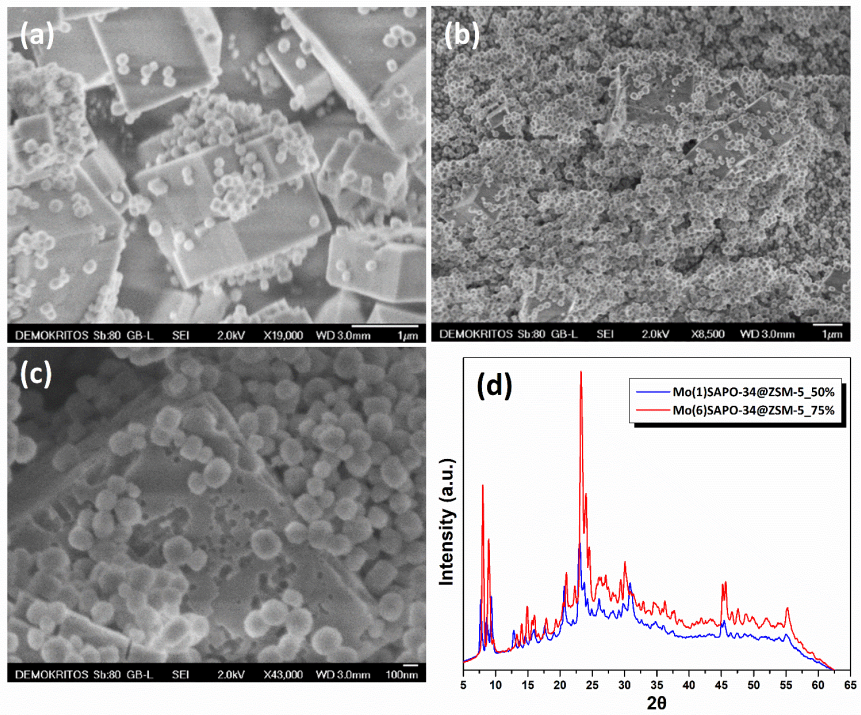

Figure 1. (**a**,**b**) SEM images of SAPO-34@ZSM-5_50% and SEM images of SAPO-34@ZSM-5_75%, respectively. (**c**) SEM image of SAPO-34@ZSM-5_75% with 6 wt% Mo content. (**d**) XRD patterns of Mo(x)SAPO-34@ZSM-5.

Figure 2a shows the N_2 adsorption isotherms at 77 K for the SAPO-34@ZSM-5 core–shell composites, alongside those of the parent SAPO-34 and Na-ZSM-5 materials. As expected, the higher BET surface area of pure SAPO-34 relative to pure Na-ZSM-5 results in the SAPO-rich composite (SAPO-34@ZSM-5_50%) exhibiting the largest surface area, reaching 533 $m^2\ g^{-1}$ (Table 1). Notably, the BET surface area of SAPO-34@ZSM-5_50% lies between those of the pristine zeolites, indicating that the ZSM-5 overgrowth does not significantly obstruct access to the SAPO-34 micropores. In contrast, when the ZSM-5 fraction is increased to 75%, the BET surface area of the resulting composite falls below that of both parent materials, suggesting partial blockage of SAPO-34 pores by the thicker ZSM-5 shell. This interpretation is further supported by the decrease in micropore volume compared with the SAPO-34@ZSM-5_50% composite as derived from the N_2 adsorption isotherm. All samples display a characteristic type-I isotherm with a hysteresis loop at relative pressures $P/P_0 = 0.9–1.0$, indicative of mesopore formation. The magnitude of this hysteresis increases with the ZSM-5 content, consistent with enhanced mesoporosity arising from crystal stacking. Upon incorporation of 1 wt% molybdenum into the composite, the decrease in BET surface area was negligible. However, as shown in the N_2 adsorption–desorption isotherm in Figure 2b, a substantial reduction in both BET surface

area and total pore volume occurred when the molybdenum loading was increased to 6 wt%. This decrease is attributed to the presence of Mo species that either diffused into the CHA pores or partially obstructed the pore entrances, as evidenced by the corresponding reduction in micropore volume for this sample. Since the conversion of ethylene to aromatics occurs on the Brønsted acid sites of the zeolite, we sought to enhance the acidity of the ZSM-5 component within the SAPO-34@ZSM-5 composite through post-synthesis ion exchange with ammonium nitrate, followed by calcination to obtain the protonated form H^+[SAPO-34@ZSM-5]. Post-synthetic protonation of the composite, which contains a higher proportion of ZSM-5, resulted in a slight increase in specific surface area to 460 m^2 g^{-1} (Figure 2a). In contrast, a pronounced decrease in specific surface area was observed for a medium Mo loading of 3 wt%, surpassing the reduction measured for the untreated sample with a higher Mo loading (Figure 2b). This trend is further confirmed by the drastic decrease in total, micropore, and mesopore volumes.

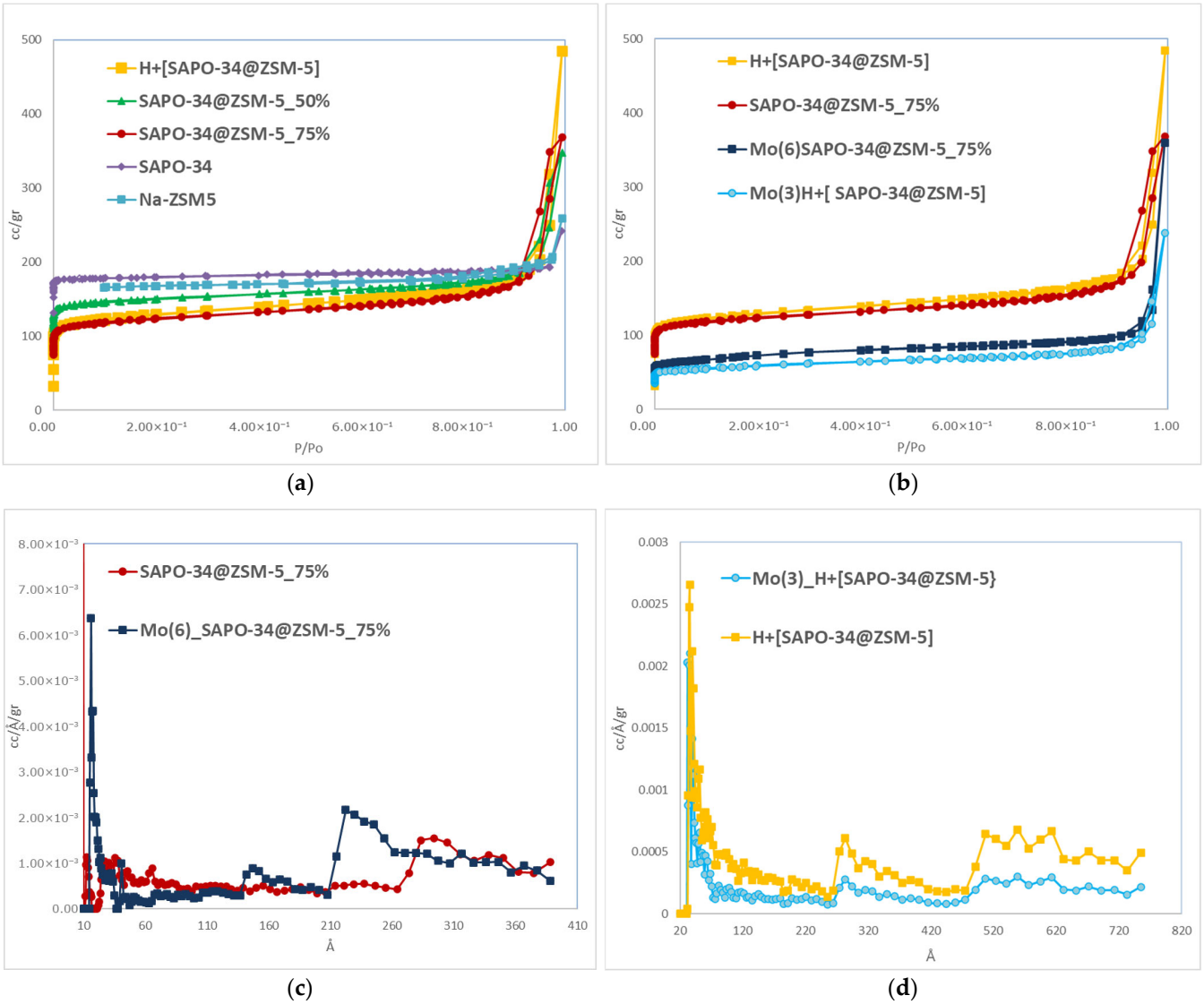

Figure 2. (**a**,**b**) N_2 adsorption/desorption isotherm branches and (**c**,**d**) pore size distribution curves of SAPO-34@ZSM-5, H^+[SAPO-34@ZSM-5] and their corresponding analogs with Mo.

Table 1. Pore structural properties of SAPO-34@ZSM-5_50%, SAPO-34@ZSM-5_75%, H$^+$[SAPO-34@ZSM-5_75%] and their corresponding analogs with Mo.

Sample	BET Surface Area (m^2/g)	Total PoreVolume cc/g	Micropore Volume cc/g	Mesopore Volume cc/g
SAPO-34	635	0.377	0.275	0.102
ZSM-5	474	0.271		
SAPO-34@ZSM-5_50%	533	0.473	0.226	0.247
SAPO-34@ZSM-5_75%	432	0.43	0.183	0.246
H$^+$[SAPO-34@ZSM-5_75%]	459	0.473	0.191	0.282
Mo(1) SAPO-34@ZSM-5_50%	437	0.34	0.185	0.155
Mo(6) SAPO-34@ZSM-5_75%	256	0.406	0.103	0.303
Mo(3)H$^+$[SAPO-34@ZSM-5_75%]	208	0.179	0.086	0.093

To evaluate the presence of hierarchical porosity in the core–shell configurations described above, we performed pore-size distribution analysis using the NLDFT method. Figure 2c,d present the pore-size distribution profiles of the composites both before and after Mo incorporation. Specifically, the curves for the composite with the highest ZSM-5 content (75%) are shown prior to and following protonation. The sample subjected to ammonium nitrate treatment exhibits an increased pore volume in both the lower mesopore range (3–4 nm) and the larger mesopore range (50–70 nm). This behavior is further confirmed by the increase in the calculated mesopore volumes. Subsequent Mo impregnation leads to a decrease in pore volume across the entire mesopore region. Nevertheless, the characteristic pore-size features are retained, suggesting that a 3 wt% Mo loading is sufficient to maintain pore accessibility for reactant molecules.

For the non-protonated composite, introduction of a high Mo loading (6 wt%) results in an increase in pore volume across the entire mesopore range, from small mesopores (~2 nm) to larger ones (~20 nm). Consistent with this observation, the mesopore volume increases from 0.246 to 0.303 cc/g upon protonation. This behavior can be attributed to the strong interaction between the Mo species and the zeolite framework within the composite. These findings are further clarified by the BET surface area data and pore-size distribution analyses for both the protonated and non-protonated SAPO-34@ZSM-5 samples, along with their corresponding Mo-loaded analogs, as summarized in Table 1.

2.1.2. Structure and Morphology of H$^+$ZSM-5@SAPO-34, and Mo(3)_H$^+$ZSM-5@SAPO-34 Synthesized by One-Step Crystallization

To mitigate catalyst deactivation and extend the operational lifetime of SAPO-34, we reduced the SAPO-34 crystal size to approximately 200 nm by employing a concentrated synthesis gel with an H_2O:Al_2O_3 ratio of 40 [31]. SEM images in Figure 3a–c show the formation of SAPO-34 on protonated ZSM-5 at various H$^+$-ZSM-5 loadings. The corresponding XRD patterns (Figure 4d) display the characteristic reflections of the CHA framework, confirming that the nanocubic SAPO-34 crystals retained their crystallinity despite the substantial reduction in particle size. However, as the proportion of H-ZSM-5 relative to SAPO-34 increased to 2:1 w/w and 3:1 w/w, the relative intensity of ZSM-5 diffraction peaks increased accordingly, indicating a higher contribution of the MFI phase in the composite material.

Figure 4a presents the N_2 adsorption–desorption isotherms of the H$^+$ZSM-5@SAPO-34 composites prepared with H$^+$ZSM-5 to SAPO-34 weight ratios of 1:1, 2:1, and 3:1. The H$^+$ZSM-5@SAPO-34[1] sample exhibits the highest BET surface area (618 m^2 g^{-1}), followed by H$^+$ZSM-5@SAPO-34[2] (530 m^2 g^{-1}) and H$^+$ZSM-5@SAPO-34[3] (511 m^2 g^{-1}). This trend suggests that increasing the SAPO-34 fraction enhances the overall microporous

contribution within the composites, a conclusion that is further supported by the corresponding micropore volume values, which follow the same trend. Notably, the BET surface areas of all composites fall between those of the corresponding parent zeolites, indicating that SAPO-34 overgrowth does not significantly impede access to the intrinsic microporosity of the ZSM-5 component.

A double hysteresis loop in the regions P/P_0 = 0.5–0.9 and P/P_0 = 0.9–1.0 is observed for the composite with the highest proportion of H^+ZSM-5, indicating the presence of two distinct mesopore domains. Figure 4b–d show the corresponding isotherms for each composite after incorporation of 3 wt% molybdenum. Among these samples, the composite with the highest SAPO-34 content exhibits the greatest reduction in specific surface area upon Mo loading, whereas the composite with the lowest SAPO-34 fraction shows the smallest decrease. A similar behavior is observed for both the micropore and mesopore volumes. This trend suggests that a higher proportion of H^+ZSM-5 in the composite facilitates a more uniform dispersion of Mo species. The BET surface areas and pore-size distribution data for H^+ZSM-5@SAPO-34[1], H^+ZSM-5@SAPO-34[2], H^+ZSM-5@SAPO-34[3], and their corresponding 3 wt% Mo-loaded analogs are summarized in Table 2.

The DFT pore-size distribution curves are displayed as insets within the corresponding N_2 adsorption–desorption isotherms for the H^+ZSM-5@SAPO-34 composites. The DFT profile of Mo(3)_H^+ZSM-5@SAPO-34[1] reveals blockage of large mesopores (>50 nm), accompanied by the formation of new mesopores with mean diameters of approximately 2 and 3.5 nm. Owing to the high SAPO-34 content in this composite, efficient dispersion of molybdenum species is hindered; consequently, migration of MoO_3 into the SAPO micropores likely generates structural defects manifested as mesopores.

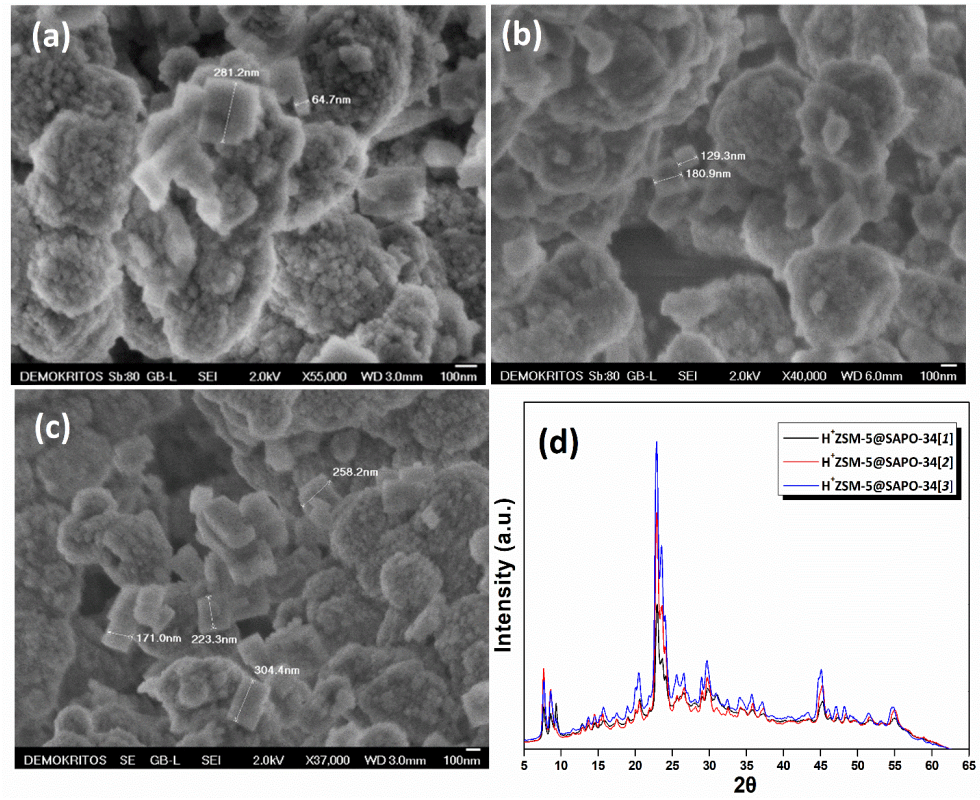

Figure 3. (**a**–**c**) SEM images and (**d**) XRD pattern of H^+ZSM-5@SAPO-34[1], H^+ZSM-5@SAPO-34[2], and H^+ZSM-5@SAPO-34[3], respectively.

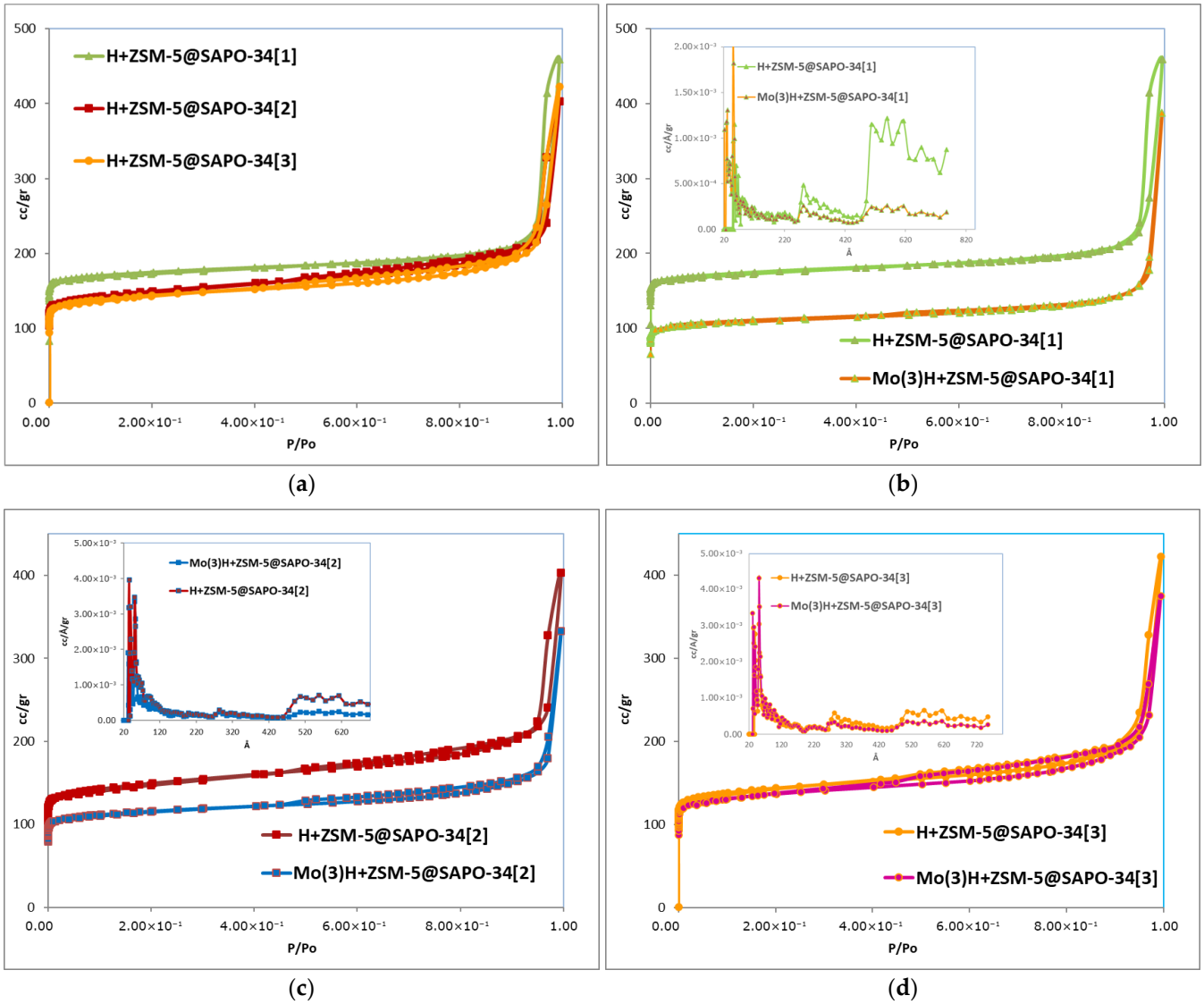

Figure 4. (**a**) N_2 adsorption/desorption isotherm branches of H^+ZSM-5@SAPO-34[1], H^+ZSM-5@SAPO-34[2], and H^+ZSM-5@SAPO-34[3] and their corresponding analogs with 3wt% Mo. (**b**–**d**) DFT pore size distribution curves.

Table 2. Pore structural properties of H^+ZSM-5@SAPO-34[1], H^+ZSM-5@SAPO-34[2] and H^+ZSM-5@SAPO-34[3] and their corresponding analogs with 3 wt% Mo.

Sample	BET Surface Area (m^2/g)	Total Pore Volume cc/g	Micropore Volume cc/g	Mesopore Volume cc/g
H^+ZSM-5	430	0.271	0.169	0.101
H^+ZSM-5@SAPO-34[1]	618	0.614	0.264	0.35
H^+ZSM-5@SAPO-34[2]	530	0.511	0.221	0.29
H^+ZSM-5@SAPO-34[3]	511	0.503	0.214	0.289
Mo(3) H^+ZSM-5@SAPO-34[1]	387	0.307	0.163	0.144
Mo(3) H^+ZSM-5@SAPO-34[2]	403	0.326	0.173	0.153
Mo(3) H^+ZSM-5@SAPO-34[3]	476	0.427	0.203	0.224

The DFT analysis of Mo(3)_H^+ZSM-5@SAPO-34[2] shows that Mo species either penetrate or obstruct pores with mean diameters of around 3.5 nm, as well as larger mesopores exceeding ~50 nm. In the case of Mo(3)_H^+ZSM-5@SAPO-34[3], the DFT pore-size distribution curve indicates the development of induced mesoporosity in the range of 3.5–5 nm following Mo incorporation. This observation is consistent with the hysteresis loop appearing in the relative pressure range of 0.45–0.1 in the corresponding N_2 isotherm. The minor reduction in pore volume across the remaining mesopore range further supports the conclusion that Mo species are highly dispersed within the composite containing the highest proportion of the H^+ZSM-5 core.

The core–shell configuration is expected to exhibit a higher specific surface area compared to a simple physical mixture, due to the intergrowth of the two zeolitic phases and the additional interfacial surface generated during secondary growth. This expectation is further supported by a theoretical estimation, in which the specific surface areas of all the composites were calculated as the weighted average of the surface areas of the individual zeolites, based on their respective mass fractions in the composite and the specific values are included in Table S2 in the Supplementary Material. In this table we provide evidence for the avoidance of isotropic self-nucleation that would conclude to a composite resembling a physical mixing of the two phases. It is clear that the experimental BET of the composites differs substantially from the weighted average of the BET specific surface areas, calculated based on the mass fraction of each phase.

Notably, the experimentally measured specific surface areas of the core–shell composites are generally higher than those predicted for the corresponding physical mixtures, indicating the beneficial effect of the core–shell architecture and the additional interfacial surface generated during secondary growth. An exception is observed in the configuration with a SAPO-34 core and a ZSM-5 shell. This behavior may be attributed to partial framework instability of SAPO-34 in this composite configuration [18,32].

The distribution of molybdenum within the protonated SAPO-34@ZSM-5_75% as well as H^+ZSM-5@SAPO-34[3] core–shell structures was examined using scanning electron microscopy coupled with energy-dispersive X-ray spectroscopy (SEM-EDS) (Figure 5a,b respectively). All Mo-containing composites exhibit a uniform spatial distribution of molybdenum, with an average loading of approximately 3 wt%. The high dispersion of Mo species on the external surface and/or within the channels of the composite zeolite H^+[SAPO-34@ZSM-5_75%] is further supported by the XRD analysis, which shows no detectable diffraction features attributable to crystalline MoO_3 (Figure 5a). The XRD patterns of all Mo(3)_H^+ZSM-5@SAPO-34 samples further corroborate the high dispersion of Mo species on the composite zeolite surface and/or within its channels, as no diffraction peaks corresponding to crystalline MoO_3 were observed in any of the three materials (Figure 5b).

To further support the absence of bulk MoO_3 in our catalysts, XRD and SEM data of a MoO_3-loaded SAPO-34 reference material are presented in the Supplementary Material (Figure S2). The XRD pattern clearly exhibits the characteristic diffraction peak of crystalline MoO_3 ($2\theta = 27.4^\circ$). The absence of such features in the XRD patterns of our composite catalysts, before and after MDA, highlights the fundamentally different dispersion state of Mo in the studied materials.

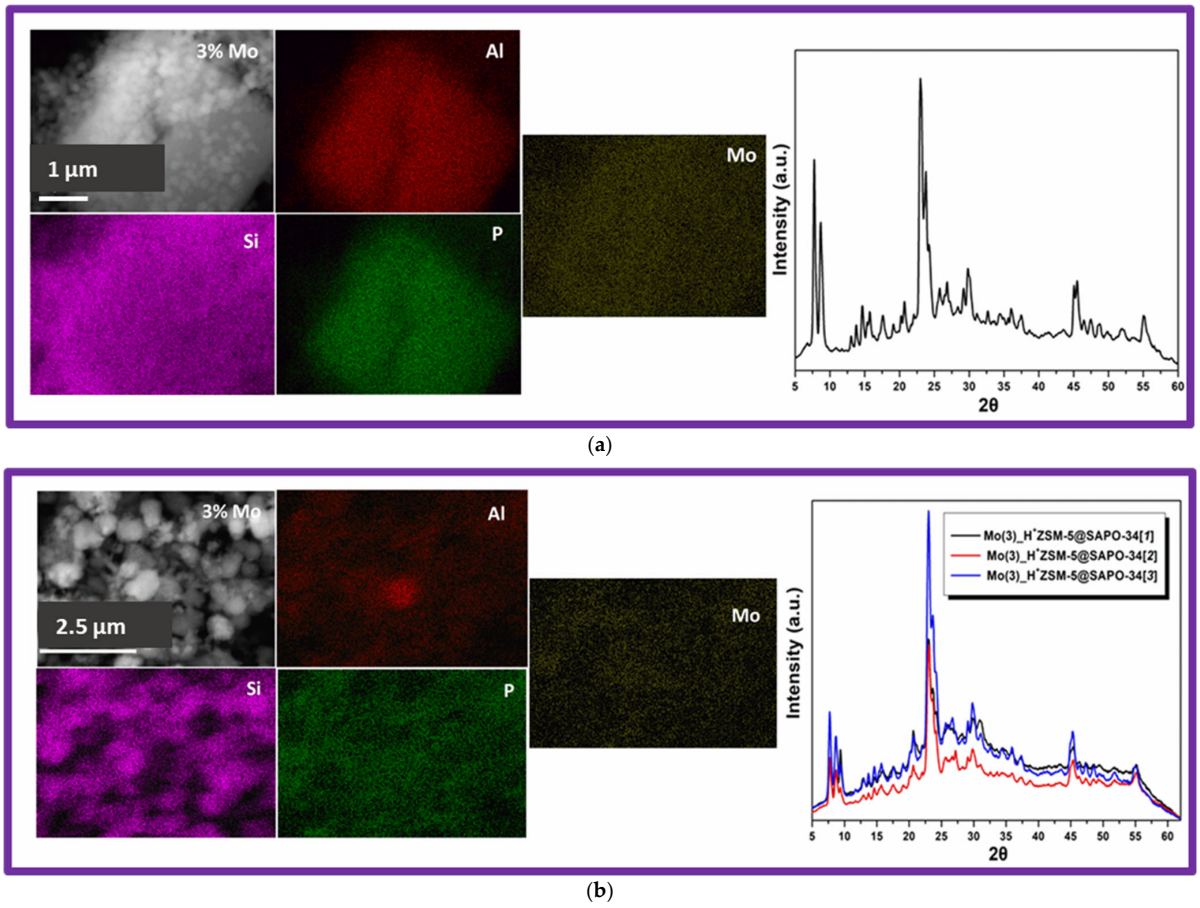

Figure 5. SEM-EDS elemental map and XRD pattern of (**a**) Mo(3)_H^+[SAPO-34@ZSM-5] and (**b**) Mo(3)_ H^+ZSM-5@SAPO-34[3]. Al (red), Si (purple), P (green), Mo (yellow).

2.1.3. Formation Mechanism of the Core–Shell Structures (Heterogeneous Nucleation)

In zeolitic systems, heterogeneous nucleation on seed crystals is well documented and is favored over homogeneous self-nucleation due to the lower nucleation energy barrier at solid surfaces. In the ZSM-5@SAPO-34 configuration, although lattice matching between the CHA and MFI frameworks is imperfect, ZSM-5 crystals possess a high density of surface silanol (Si-OH) and aluminol (Al-OH) groups. Under hydrothermal synthesis conditions, these surface hydroxyls act as anchoring sites for SAPO species, promoting preferential nucleation of SAPO-34 on the ZSM-5 surface. Once initial SAPO-34 nuclei are formed, secondary crystal growth proceeds, leading to partial shell coverage driven by surface energy minimization and chemical compatibility of aluminosilicate frameworks. In the reverse synthesis route (SAPO-34@ZSM-5), where presynthesized SAPO-34 crystals are introduced into the ZSM-5 reaction solution, the instability of the SAPO framework under the strongly alkaline conditions of ZSM-5 synthesis necessitates surface functionalization of SAPO-34 with TPABr. This treatment suppresses bulk self-nucleation and promotes preferential crystallization of the shell phase on the core SAPO-34 surface [33–35].

2.1.4. Acidic Properties of SAPO-34, Na-ZSM-5, SAPO-34@ZSM-5, and Mo(x) SAPO-34@ZSM-5

The NH_3-TPD patterns of parent zeolites, as well as the composites before and after loading with Mo, are shown in Figure 6a. SAPO-34 demonstrates a profile with two distinct peaks at approximately 195 °C and 430 °C, indicating the presence of both weak Lewis acid sites at the lower temperature and mainly Brønsted acid sites at the higher temperature [36,37]. In contrast, the NH_3-TPD profile of Na-ZSM-5 shows a single broad

peak centered around 220 °C, suggesting predominantly weak acidity [38]. The growth of Na-ZSM-5 shell over SAPO-34 completely transformed the acidity of the substituent zeolites This modification primarily affected the Brønsted acid sites, as evidenced by the reduced intensity and a shift in the high-temperature desorption peak from 430 °C to 395 °C, along with the appearance of a more pronounced desorption peak at 195 °C. The reduced intensity in the high-temperature region, confirms the absence of strong Brønsted acid sites in the shell attributed to the absence of protonation [18,21]. Consequently, the acidity in this composite arises mostly from the SAPO-34 core, with only a minor and relatively weak contribution from the shell. Modification of the composite zeolitic material by Mo (1 wt%) resulted in the preservation of the intrinsic acidity of the composite, particularly the strong Brønsted acid sites. The observed increase in weak Lewis acidity upon Mo addition is according to previous studies, related to the presence of highly dispersed MoO_3 species on the zeolite surface dispersion degree [39,40]. The composite with the highest Mo content exhibits a further noticeable decline in strong basic acid sites, as indicated by the shift in the high temperature desorption peak from 395 °C to 370 °C and the pronounced decrease in its desorption area [41]. This suggests that the increased amount of active Mo species results in a partial loss or masking of these acid sites. Concurrently, there is a rise in weak acid sites. These results are consistent with the findings from XRD and SEM analysis.

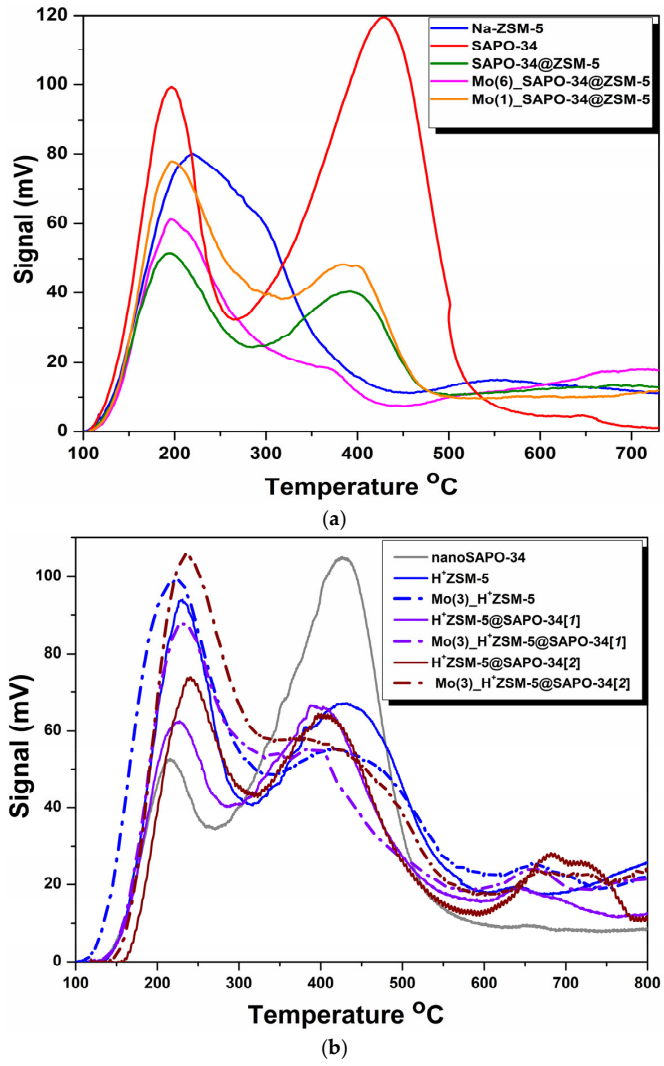

Figure 6. NH_3-TPD curves of (**a**) SAPO-34, Na-ZSM-5, SAPO-34@ZSM-5, and Mo(x)_SAPO-34@ZSM-5 where x = 1 and 6 wt%, (**b**) nanoSAPO-34, H^+ZSM-5, SAPO-34@ZSM-5 (1:1 *w*/*w*), SAPO-34@ZSM-5 (1:2 *w*/*w*), and their corresponding analogs with 3 wt% Mo.

2.1.5. Acidic Properties of H^+ZSM-5, nanoSAPO-34, H^+ZSM-5@SAPO-34, and Mo(x)_H^+ZSM-5@SAPO-34

The influence of the H^+ZSM-5 proportion, as well as the metal loading, on the acidity of composite zeolitic catalysts containing commercial protonic ZSM-5 as the core was examined [42]. The NH_3-TPD profiles shown in Figure 6b display two desorption peaks at approximately 200 °C and 400 °C, corresponding to the weak and strong acid sites of SAPO-34 and ZSM-5, respectively [43].

Compared with the parent zeolites, the H^+ZSM-5@SAPO-34 composites exhibit a reduced fraction of strong acid sites, accompanied by a shift in the high-temperature peak to lower temperatures. Additionally, both the total acidity and acid strength of the composites increase with increasing ZSM-5 content [44,45]. Upon Mo incorporation, the composites show an increase in weak Lewis acidity and a concomitant decrease in strong Brønsted acidity, along with a shift in the corresponding desorption peak to lower temperatures. This behavior is attributed to the reaction of sublimed Mo oxide species with Brønsted sites and is most pronounced in the composite with the highest H^+ZSM-5 proportion.

2.2. Catalytic Performance on Mo-Supported Integrated Structures

The catalytic performance of the three types of bifunctional catalysts was evaluated at 700 °C over a reaction period of 10 h, examining the effects of Mo loading, the relative proportions of SAPO-34 and ZSM-5, and the overall acid strength. The activity of all core–shell composites was benchmarked against commercially available acidic ZSM-5 (Si/Al = 12) to assess the impact of the core–shell architecture on catalytic behavior. Before proceeding with the presentation of the results, it must be emphasized that the MDA reaction is thermodynamically limited, and the maximum methane conversion depends strongly on temperature and the equilibrium constant at that temperature. At industrially relevant temperatures (~700 °C), thermodynamic calculations show that maximum methane conversion rarely exceeds 12% under atmospheric pressure, even with ideal catalysts. Real catalysts achieve even lower conversions (<10–12%) due to coking, side reactions, and kinetic limitations, so thermodynamics sets the upper limit, but catalyst performance usually determines the actual conversion.

2.2.1. Catalytic Performance of Mo(x)_SAPO34@ZSM-5 and Mo(x)_H^+[SAPO34@ZSM-5] and Mo(x)_H^+ZSM-5@SAPO-34

SAPO-34@ZSM-5 (SAPO-34 core, ZSM-5 shell):

Figure 7 presents the temporal profiles of CH_4 conversion (Figure 7a) and benzene yield (Figure 7b) over SAPO-34@ZSM-5 composites loaded with 1, 3, and 6 wt% Mo, as well as the protonated counterpart containing 3 wt% Mo. All catalysts exhibit a similar trend, with a pronounced decline in methane conversion after approximately 160 min, followed by a gradual decrease until the end of the reaction. This reduction in methane conversion is accompanied by a corresponding decrease in benzene yield. Notably, the reference protonated ZSM-5-supported Mo catalyst achieves the highest benzene yield among all tested materials. In contrast, all non-protonated SAPO-34@ZSM-5 composites display low activity in both methane conversion and benzene formation, regardless of Mo loading. These observations suggest that the nature of active Mo species on SAPO-34@ZSM-5 differs from those on H^+ZSM-5 [38]. The relatively mild acidity of the composite, resulting from the growth of a non-protonated ZSM-5 shell over the SAPO-34 core, as confirmed by NH_3-TPD analysis, likely causes the Mo species to remain primarily as MoO_3. These species are either dispersed on the external surface of the zeolite crystals or, in smaller form, partially penetrate the ZSM-5 channels during calcination, independent of Mo loading [46]. The small size of these molybdenum oxide species is further supported by their absence in the XRD patterns.

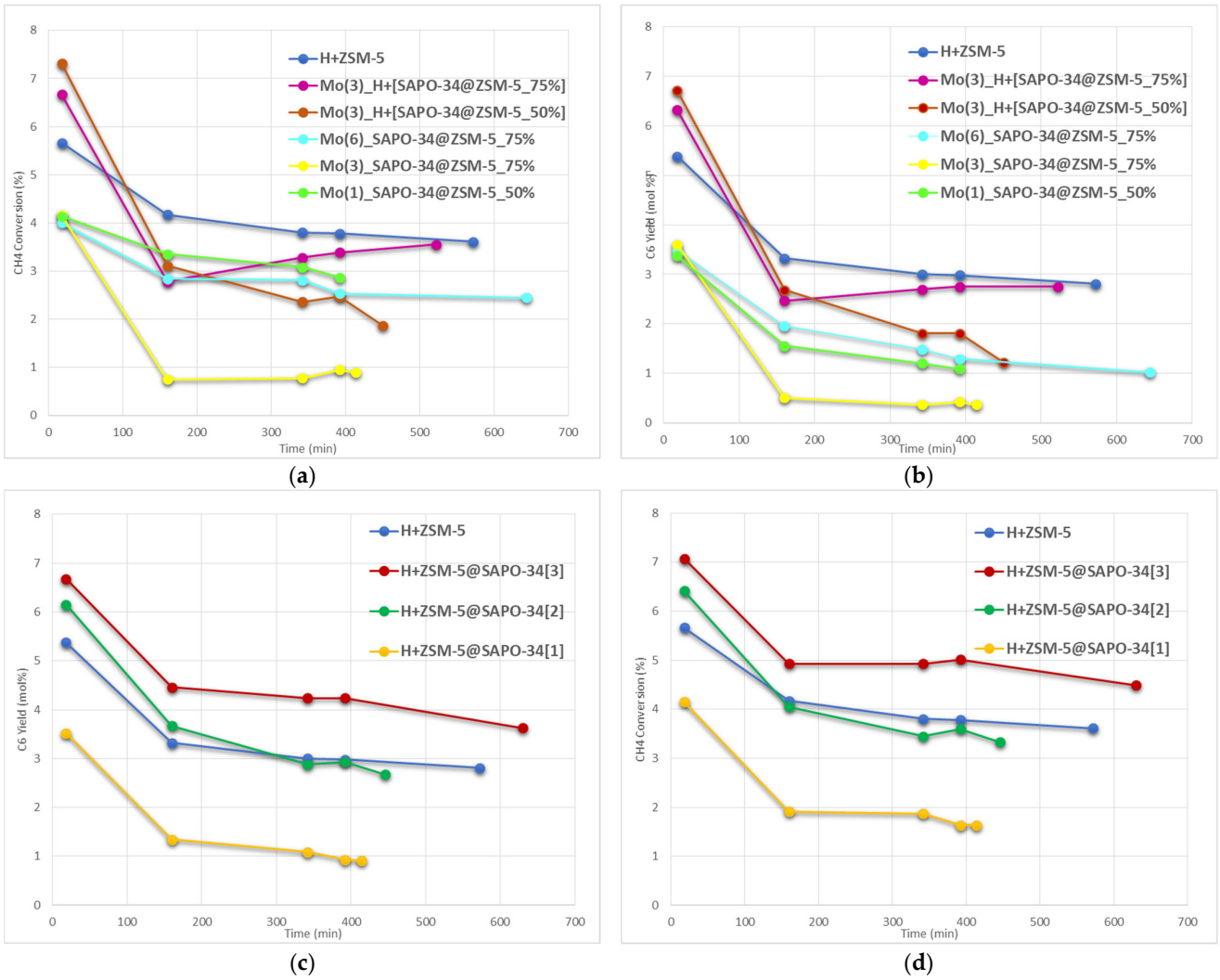

Figure 7. (**a**) Methane conversion efficiency at 700 °C and (**b**) benzene yield of SAPO-34@ZSM-5 of 1,3, and 6 wt% and Mo(3)_H^+[SAPO-34@ZSM-5] (**c**) Methane conversion efficiency at 700 °C and (**d**) benzene yield of H^+ZSM-5@SAPO-34 of 3 wt% Mo.

It is well established that the catalytic activity of zeolites is closely related to the location of Mo species within the zeolite framework [47,48]. The reducibility of Mo species varies depending on their position within H^+ZSM-5. Specifically, Mo species located within the zeolite channels, associated with Brønsted acid sites, exhibit higher effectiveness in methane activation and are less prone to carbon deposition compared to Mo species not associated with these sites. In contrast, MoO_3 species not linked to Brønsted acid sites tend to convert into Mo carbide species. Among these, the MoC_xO_y species associated with Brønsted acid sites display higher stability and activity than those formed elsewhere [49]. Another factor that adversely affects the performance of SAPO-34@ZSM-5 composites is the loss of zeolite crystallinity resulting from the migration of MoO_x species into the SAPO micropores. This phenomenon is corroborated by the pore-size distribution analysis in Figure 2c, which shows increased pore volume across the mesopore range, particularly in composites with higher SAPO content, as further evidenced by the XRD patterns in Figure 1. Protonation of the composite clearly enhances initial methane conversion and benzene yield, bringing performance levels close to those of the reference sample. This improvement reflects a successful enhancement of both acidity and Mo dispersion. However, both protonated composites, despite varying ZSM-5-to-SAPO weight ratios, exhibit a pronounced decline

in activity over time, indicating catalyst deactivation and suggesting that the intended Brønsted acidity may not have been fully realized.

H^+ZSM-5@SAPO-34 (H^+ZSM-5 core, SAPO-34 shell):

After establishing that a 3 wt% Mo loading represents the optimal metal concentration for enhancing catalytic activity without compromising the SAPO-34 zeolite structure, and considering that ZSM-5 possesses higher acidity with Brønsted acid sites critical for finer Mo dispersion and the promotion of aromatization reactions, we evaluated the catalytic performance of three H^+ZSM-5@SAPO-34 core–shell structures with mass ratios of 1:1, 2:1, and 3:1, each loaded with 3 wt% Mo. The corresponding results are presented in Figure 7c,d.

Methane conversion and benzene yield over all H^+ZSM-5@SAPO-34 configurations exhibited the characteristic gradual decline over reaction time. Both metrics increased with higher H^+ZSM-5/SAPO-34 mass ratios, reflecting the increasing number of Brønsted acid sites, as confirmed by NH_3-TPD analysis [45]. This indicates that a higher proportion of ZSM-5 in the core–shell architecture has a strongly beneficial effect on both methane conversion and benzene yield, surpassing the performance of the reference H^+ZSM-5 catalyst.

As widely recognized, the key factors governing the catalytic performance of zeolite molecular sieves are pore architecture and acid strength. In the 3:1 H^+ZSM-5@SAPO-34 composite, the higher ZSM-5 content provides an increased number of strong anchoring sites, promoting the migration and uniform distribution of MoO_x species within the zeolite channels. Furthermore, N_2 physisorption results indicate that the combination of MFI and CHA topologies at this mass ratio establishes a finely interconnected micro/mesopore network, facilitating more uniform Mo dispersion and enhanced product formation. In contrast, the same type of composite with a higher proportion of SAPO-34, i.e., Mo(3)_H^+ZSM-5@SAPO-34[1], exhibits the lowest benzene yield. This observation aligns with BET surface area analyses, confirming that an excess of SAPO-34 in the integrated structure impedes effective Mo distribution and access to active sites.

2.2.2. Core–Shell Effect on Cumulative Product Yield and Benzene Selectivity

Figure 8 presents the cumulative product yields, expressed per gram of catalyst, for the major hydrocarbon species formed over a 10 h reaction period for both core–shell composite types. In all cases, benzene was the dominant product. Ethylene was consistently observed as the key intermediate of the MDA reaction across both composite types and for all Mo loadings. Modest quantities of propylene were detected in some instances, whereas toluene formation remained consistently low for all samples. Notably, naphthalene was detected exclusively in catalytic tests involving samples with higher ZSM-5 content (i.e., 100% and 75%).

These findings confirm that increasing the density of acidic sites was a step in the right direction. The untreated catalyst, Mo(3)_SAPO-34@ZSM-5_75%, exhibited a relatively low benzene yield but a markedly high ethylene yield, comparable to that of the reference sample. In contrast, its protonated analog delivered the highest cumulative benzene yield among all SAPO-34@ZSM-5-type core–shell configurations, along with a simultaneous decrease in ethylene yield. A consistent enhancement in benzene formation was observed across all H^+ZSM-5@SAPO-34 composites, which also exhibited complete suppression of naphthalene formation.

The Mo(3)_H^+ZSM-5@SAPO-34[1] sample produced a substantial amount of ethylene, attributable to its elevated SAPO content. This characteristic also explains the increased accumulation of carbonaceous deposits on this catalyst relative to other samples in the same series, as confirmed by TGA measurements. It should additionally be noted that the comparatively lower productivity of Mo(3)_H^+ZSM-5@SAPO-34[3], as indicated by cumulative yields, may be partly due to the fact that all samples were tested in their as-prepared powder form, without pelletization, crushing, or sieving. Since cumulative

yield is normalized to catalyst mass, the higher mass of this particular sample may have promoted channeling phenomena in the reactor, reducing the effective utilization of the catalyst bed.

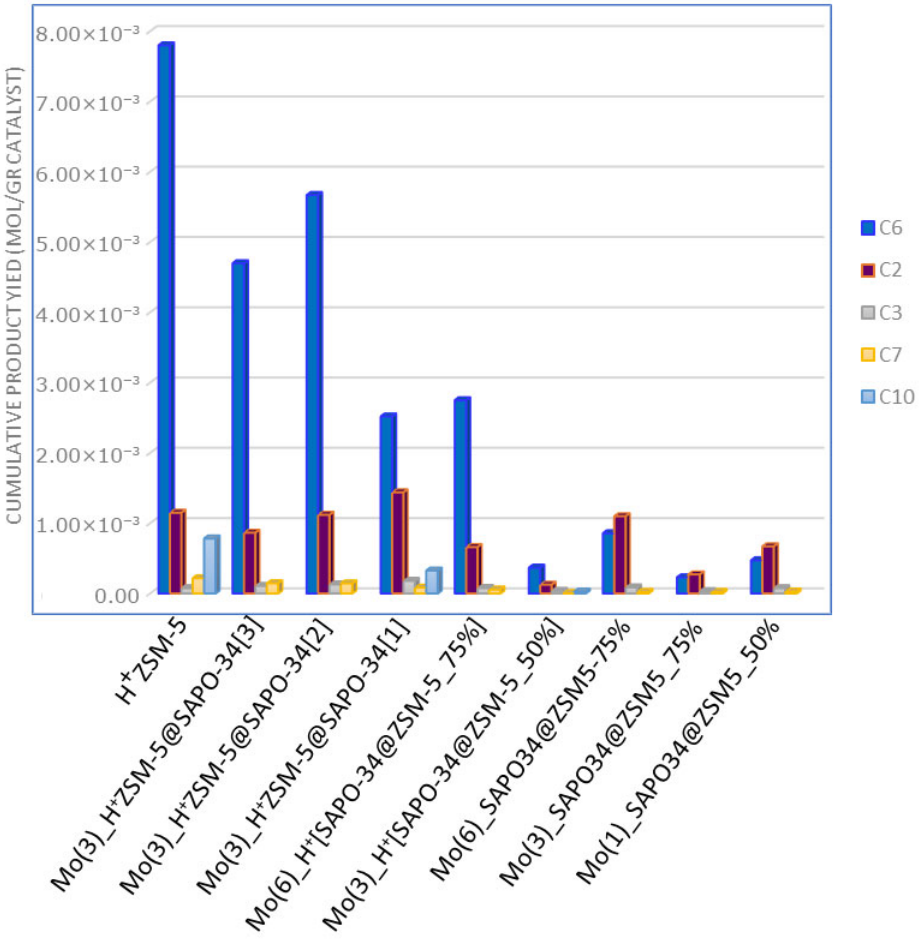

Figure 8. Cumulative yield of HC products per mass of catalyst for SAPO-34@ZSM-5 of 1, 3, 6 wt% Mo, H⁺[SAPO-34@ZSM-5], and H⁺ZSM-5@SAPO-34 of 3 wt% Mo.

SAPO-34 exerts a pronounced influence on the reaction environment in both ZSM-5@SAPO-34 and SAPO-34@ZSM-5 composite catalysts, fulfilling a dual function. First, its small pore size induces a confinement effect that favors ethylene formation over heavier hydrocarbons, thereby limiting excessive hydrocarbon chain growth and mitigating coke accumulation. Second, due to its moderate Brønsted acidity relative to aluminosilicate ZSM-5, SAPO-34 modulates the overall acidity of the composite catalyst, helping to suppress overcracking and subsequent coking.

Figure 9 illustrates the benzene and ethylene selectivity profiles for the SAPO-34@ZSM-5, H⁺[SAPO-34@ZSM-5], and H⁺ZSM-5@SAPO-34 catalytic composites. Benzene selectivity for H⁺ZSM-5 and all protonated composites—particularly H⁺ZSM-5@SAPO-34[3], H⁺ZSM-5@SAPO-34[2], and H⁺[SAPO-34@ZSM-5_75%], each loaded with 3 wt% Mo—initially exhibited very high values, gradually declining to approximately 80% after 10 h on stream. The next-highest initial benzene selectivity was observed for Mo(3)_H⁺[SAPO-34@ZSM-5_50%].

Among all protonated materials, the most pronounced decline over time occurred in those subjected to post-synthesis protonation. In contrast, H⁺ZSM-5@SAPO-34[3] and H⁺ZSM-5@SAPO-34[2] maintained high and nearly constant benzene selectivity throughout the reaction, a trend also observed for pure H⁺ZSM-5.

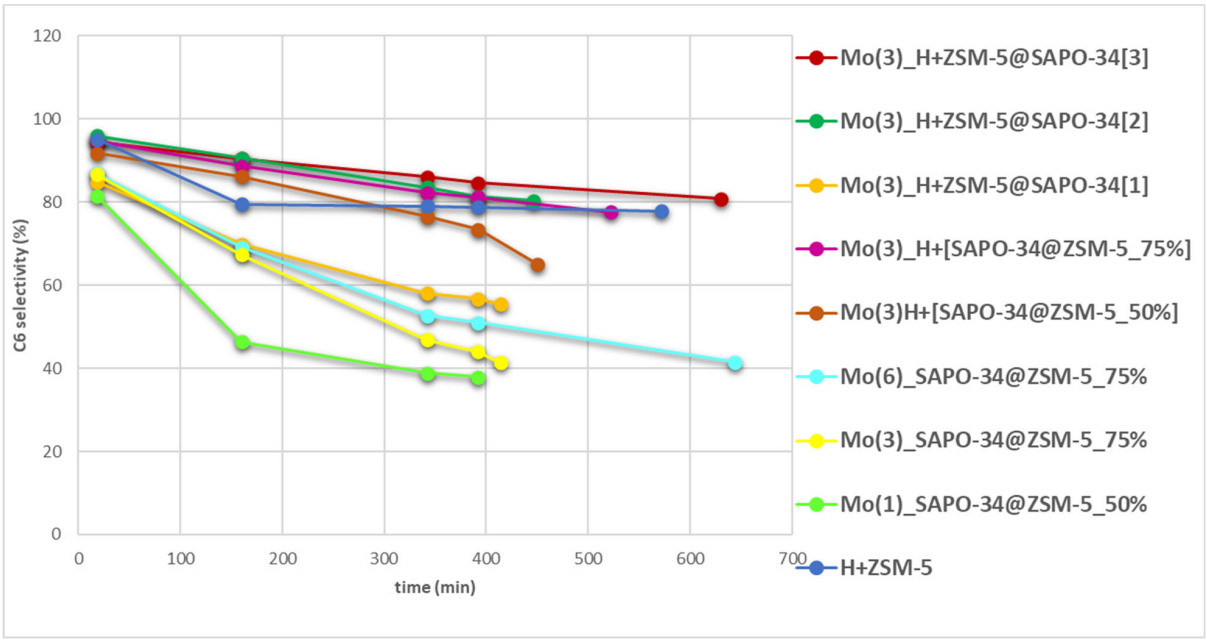

(**a**)

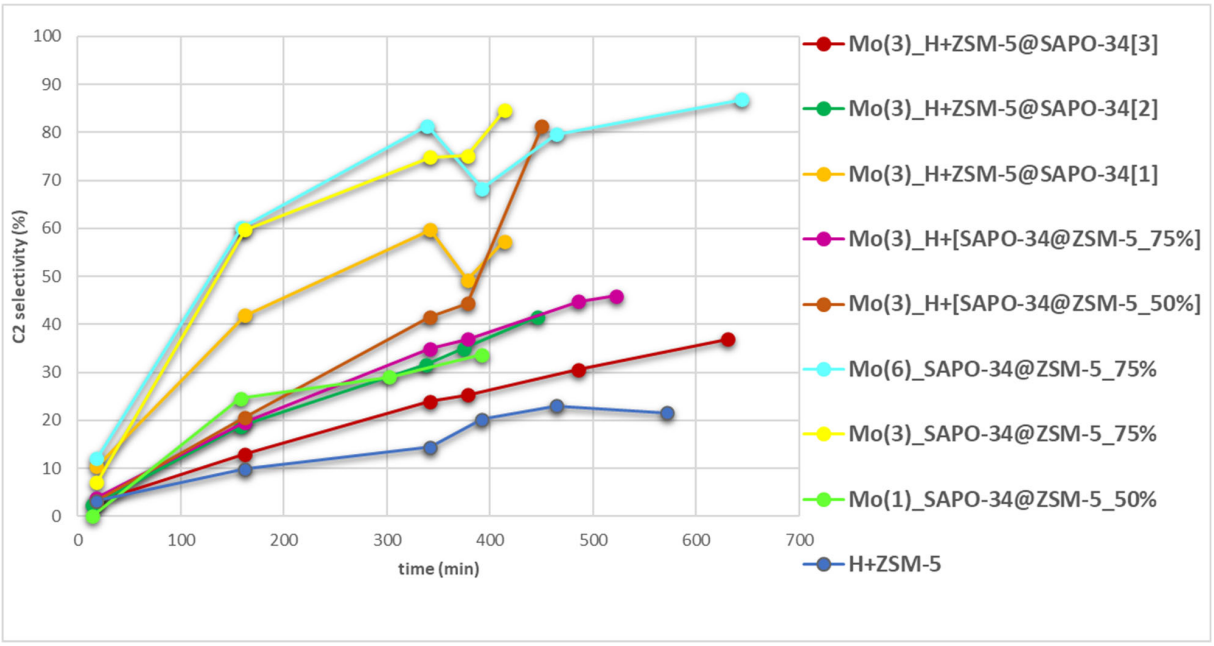

(**b**)

Figure 9. (**a**) Benzene and (**b**) ethylene selectivity values of SAPO-34@ZSM-5, H^+[SAPO-34@ZSM-5], and H^+ZSM-5@SAPO-34 conformations.

Across all composites, benzene and ethylene selectivity displayed an inverse relationship: lower ethylene selectivity consistently corresponded to higher benzene selectivity. SAPO-34@ZSM-5 samples, as well as H^+ZSM-5@SAPO-34[1], exhibited the lowest initial benzene selectivity and the most substantial decline over time. These same catalysts displayed the highest ethylene selectivity, indicating that ethylene accumulates due to limited secondary conversion pathways, thereby accounting for their poor benzene selectivity.

Overall, composites possessing higher acidity facilitate the immobilization of MoO_x species within the zeolite pores, enabling the shape-selective environment of ZSM-5 to drive benzene formation. Regarding the role of SAPO-34 in post-protonated materials, particularly those with a high ZSM-5 shell content, the SAPO-34 core provides a well-balanced catalytic response: it offers moderate ethylene and benzene selectivity and exhibits a slower

deactivation rate compared to pure H^+ZSM-5. Conversely, when SAPO-34 forms the shell around protonated ZSM-5—as in the H^+ZSM-5@SAPO-34[3] and H^+ZSM-5@SAPO-34[2] systems—ZSM-5 effectively retains ethylene within the pore network and promotes its further transformation into aromatics [50]. As a result, these catalysts display consistently low ethylene selectivity, accompanied by notably high benzene selectivity [51].

The selectivity ranking confirms that H^+ZSM-5@SAPO-34[3] delivers the highest benzene yield, surpassing even the benchmark H^+ZSM-5 at the same Mo loading. This demonstrates that an optimal SAPO-34 content combined with protonated ZSM-5—achieved most effectively in the H^+ZSM-5@SAPO-34 architecture—promotes highly efficient and selective ethylene-to-benzene conversion. Moreover, this configuration suppresses side reactions, leading to heavier aromatics such as naphthalene, which appears in appreciable amounts only for the pure ZSM-5 sample and is known to accelerate coke formation and catalyst deactivation. The enhanced stability is attributed to the confined acidic environment provided by SAPO-34, which limits secondary reactions and prolongs catalyst lifetime. The representative benzene selectivity values of all tested catalysts are summarized in the Supplementary Materials (Table S1).

2.3. Characterization of Spent Catalysts

2.3.1. Study on the Amount of the Carbonaceous Deposits Formed on Mo-Supported Catalysts (3 wt% Mo) by TGA

Thermogravimetric analysis (TGA) was carried out on H^+ZSM-5@SAPO-34 and H^+[SAPO-34@ZSM-5], both loaded with the same Mo content, over the temperature range of 30–700 °C. The total weight loss was used to quantify the amount of coke deposited on each catalyst. As shown in Figure 10, all catalysts exhibit a pronounced weight loss between 400 and 630 °C, corresponding to the combustion of carbonaceous deposits.

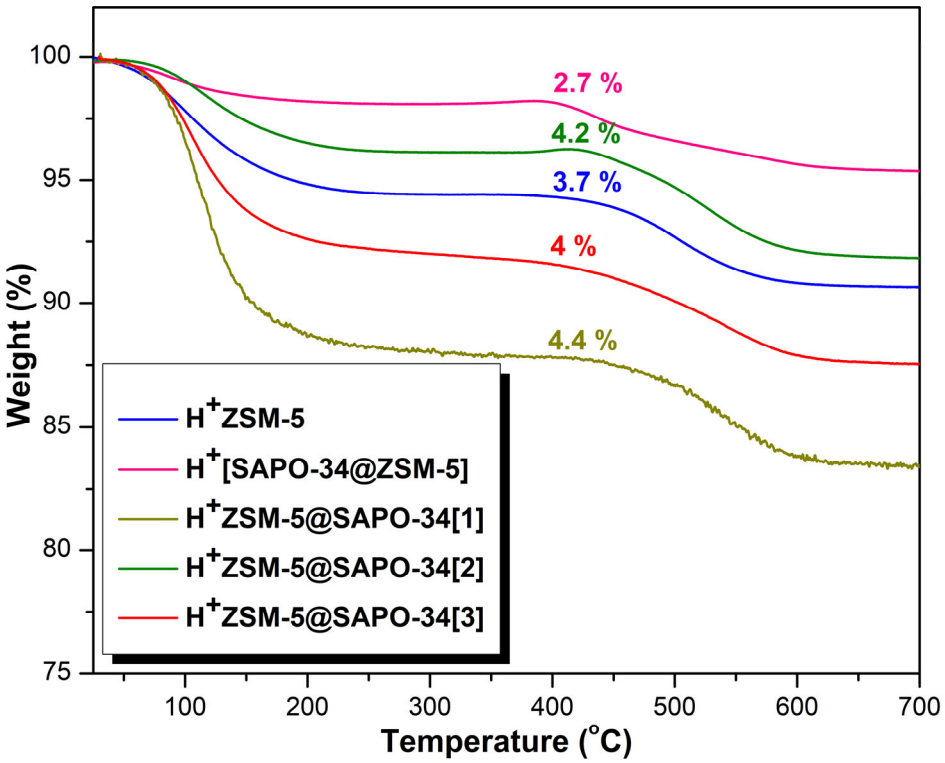

Figure 10. TGA curves of H^+ZSM-5 (blue line), H^+ZSM-5 @ SAPO-34[1] (olive green line), H^+ZSM-5@SAPO-34[2] (green line), H^+ZSM-5@SAPO-34[3] (red line), and H^+[SAPO-34@ZSM-5] (pink line). All samples are loaded with 3 wt% Mo.

For all composites incorporating H^+ZSM-5 as the core, the coke content increases as the proportion of H^+ZSM-5 decreases. The highest weight loss (4.4%) was recorded for H^+ZSM-5@SAPO-34[1], indicating a larger amount of coke on the catalyst with the lowest acidity and the highest ethylene yield. A slight increase in mass below 450 °C—most evident for the H^+ZSM-5@SAPO-34[2] composite—is attributed to the oxidation of MoC_x species [46,52].

Among all protonated zeolites, the post-synthesis protonated sample exhibited the lowest coke formation, reflecting its reduced catalytic activity compared to the composites containing H^+ZSM-5 in their initial composition.

2.3.2. XRD Analysis of the Spent Catalysts

Figure 11 presents the XRD patterns of the spent catalysts with the two core–shell configurations. For the SAPO-34@ZSM-5 composite with high Mo loading (Figure 11a), a notable decrease in crystallinity is observed after the reaction. This decline is likely caused by mild framework degradation, particularly desilication of the SAPO core, combined with increased coke deposition, with both effects being associated with higher Mo content. The SEM image in the inset of Figure 11b further supports the hypothesis of SAPO framework destabilization following the reaction.

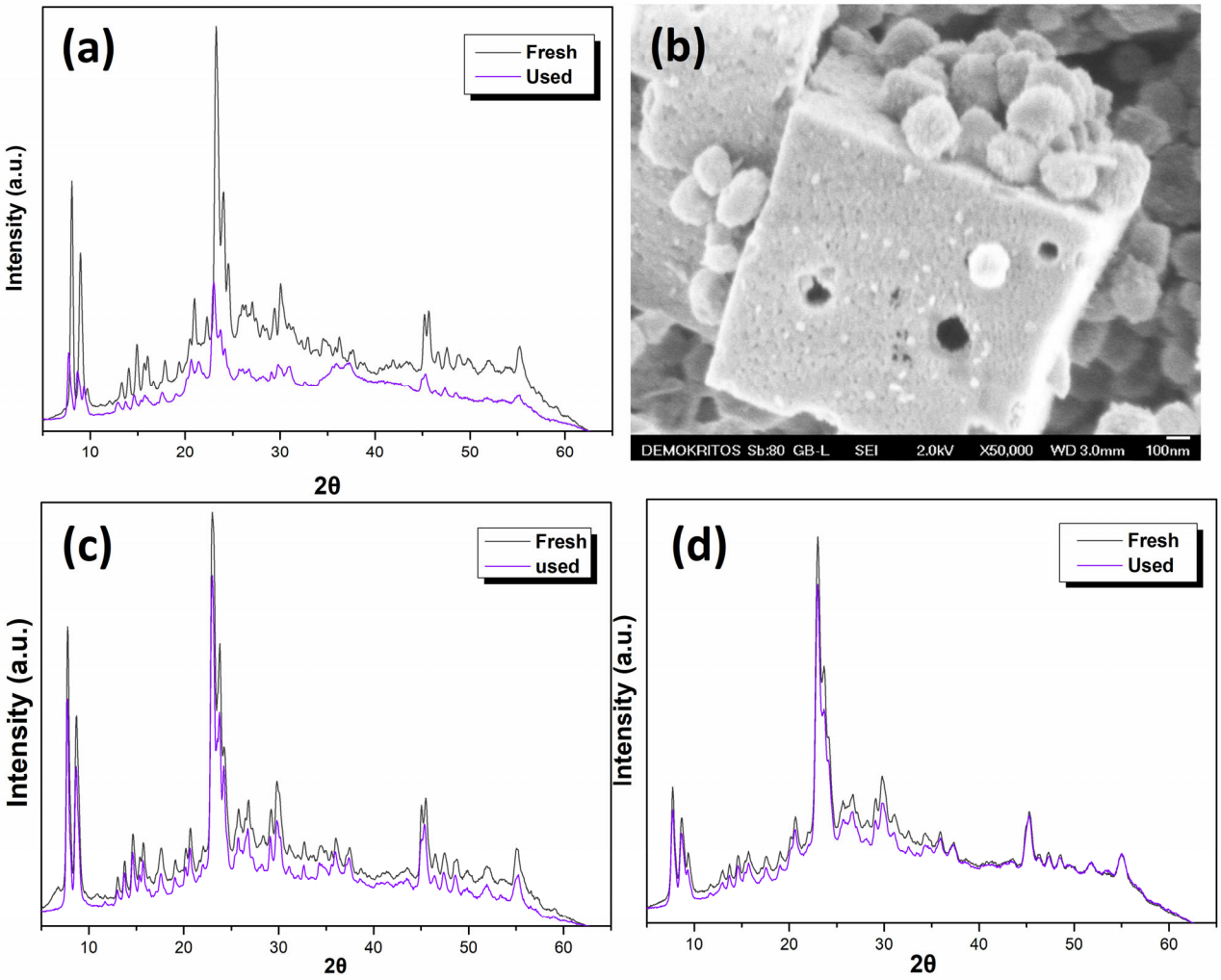

Figure 11. (**a**–**d**) XRD patterns of Mo(6)_SAPO-34@ZSM-5_75%, Mo(3)_H^+[SAPO-34@ZSM-5_75%], and Mo(3)_H^+ZSM5 @ SAPO34[3] spent catalysts, respectively. (**b**) SEM image of spent Mo(6)_SAPO-34@ZSM-5_75%.

Figure 11c,d show the XRD patterns of the protonated forms of the two core–shell configurations. Both catalysts preserved their crystallinity after the MDA reaction, indicating strong thermal and chemical stability under the harsh reaction conditions. However, the Mo(3)_H^+[SAPO-34@ZSM-5_75%] sample (Figure 11c) exhibits a slightly greater reduction in peak intensity, particularly at higher 2θ angles. This may be attributed to stronger metal–support interactions on the external, protonated ZSM-5 shell. Additionally, the absence of Mo carbide diffraction peaks in all XRD patterns, even for the non-protonated sample, suggests effective Mo dispersion across all configurations.

3. Materials and Methods

3.1. Synthetic Procedure for Obtaining SAPO-34 and ZSM-5 and Integrated Core/Shell Configurations

3.1.1. Synthesis of SAPO-34 and ZSM-5

SAPO-34 core crystals were prepared from precursor solution of the following molar composition: Al_2O_3:P_2O_5:SiO_2:TEAOH:H_2O = 1:2:0.6:4:100. A given amount of TEAOH (35 wt% in water, Sigma-Aldrich, St. Louis, MO, USA) was first dissolved in DI water. Then aluminum isopropoxide powder (98%, Sigma-Aldrich, St. Louis, MO, USA) was added to the TEAOH solution under vigorous stirring for 2 h. Then orthophosphoric acid, (H_3PO_4) solution (85 wt%, Merck, Darmstadt, Germany) and silica sol (40 wt% in water, Sigma-Aldrich, St. Louis, MO, USA) were added dropwise under stirring, and the mixed solution was aged for 12 h, hydrothermally treated at 175 °C for 48 h, and then quenched to room temperature. The ZSM-5 reacting mixture was prepared by dissolving NaOH (Sigma-Aldrich, St. Louis, MO, USA) in tetrapropylammonium hydroxide solution (TPAOH) (1.0 M in water, Sigma-Aldrich, St. Louis, MO, USA), together with water and aluminum isopropoxide. Tetraethyl orthosilicate (TEOS) (98%, Sigma-Aldrich, St. Louis, MO, USA) was then added to this solution. The molar ratio of the resulting ZSM-5 precursor solution was Al_2O_3:SiO_2:TPAOH:Na_2O:H_2O = 1:50:10:7.11:5000. The suspension obtained was maintained under mechanical agitation for 2 h at room temperature. Then the mixture was hydrothermally treated at 175 °C for 24 h and then quenched to room temperature. The solid obtained by centrifugation was washed with deionized water and then dried at 80 °C overnight [24].

3.1.2. Synthesis of SAPO-34@ZSM-5 Core/Shell Configuration via One-Step Crystallization

The as-synthesized SAPO-34(TEAOH) was ion-exchanged with 1 M TPABr (Sigma-Aldrich, St. Louis, MO, USA) propanolic solution (Merck, Darmstadt, Germany) to obtain a TPA^+-functionalized SAPO-34. The TPA-SAPO-34 was fully mixed with ZSM-5 synthesis solution of molar composition Al_2O_3:SiO_2:TPAOH:Na_2O:H_2O:EtOH = 1:100:24:0.4:1920:400 and then transferred to a Teflon-lined stainless-steel autoclave for 60 h hydrothermal treatment at 100 °C. The product was collected and purified in a similar manner to that of the parent zeolites. Calcined ZSM-5@SAPO34 was placed in hydrogen form by converting it initially to ammonium form by ion exchange in 1 M NH_4NO_3 (Sigma-Aldrich, St. Louis, MO, USA) solution at 80 °C for 12 h and then activated in flowing dry air at 500 °C for 5 h. Samples before and after the protonation treatment are denoted as SAPO-34@ZSM-5 and H^+ [SAPO-34@ZSM-5], respectively [17].

3.1.3. Synthesis of ZSM-5@SAPO-34 Core/Shell Configuration via One-Step Crystallization

Commercial protonated ZSM-5 zeolite with a Si:Al molar ratio of 12 denoted as P20-n (ACS Material, Pasadena, CA, USA), was also employed as a core structure. Different amounts of H-ZSM5 (0.2, 1, and 2 g) were mixed with SAPO-34 slurry of molar composition

Al_2O_3:P_2O_5:SiO_2:TEAOH:H_2O = 1:1:0.6:2:40 and then transferred to a Teflon-lined stainless-steel autoclave for a 48 h hydrothermal treatment at 175 °C. The composite is denoted as H^+ZSM-5@SAPO-34. The synthetic procedures for obtaining H^+ZSM-5@SAPO-34 and SAPO-34@ZSM-5 composites through one-step crystallization are graphically depicted in Scheme 1 [31].

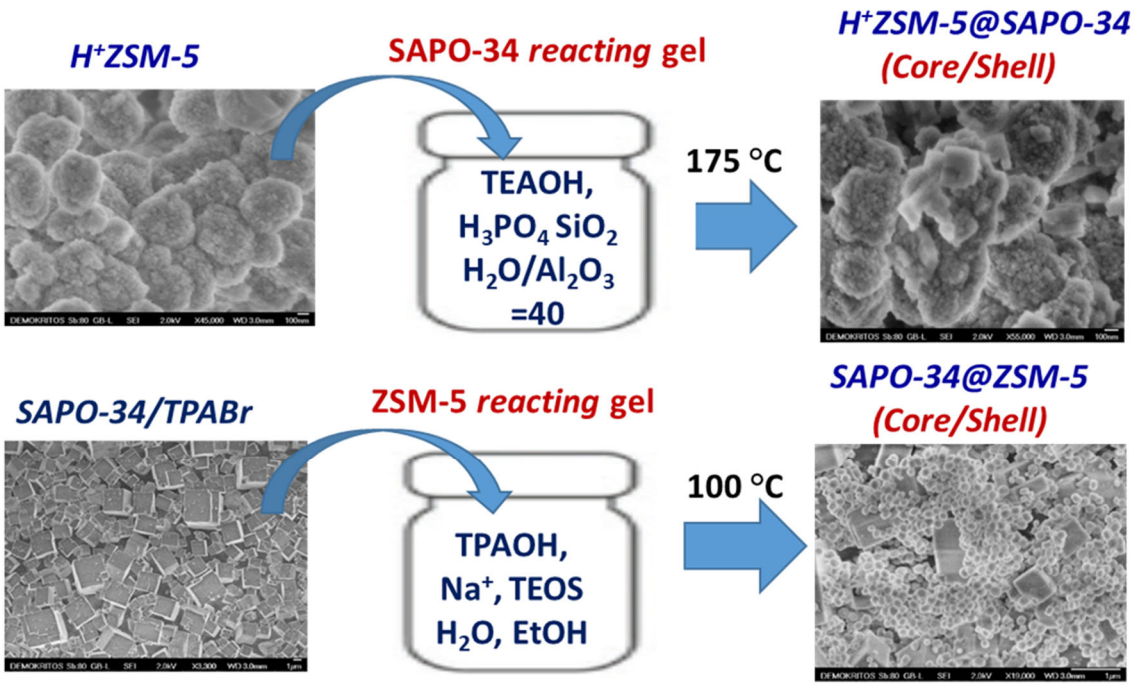

Scheme 1. Schematic illustration of core–shell structures obtained by one-step crystallization.

3.1.4. Preparation of Mo-Supported Catalysts

Mo-supported catalysts were prepared by the wet impregnation technique by adding 0.5 g of calcined zeolites to 20 mL of distilled water and adding 20 mL of an aqueous solution containing the desired amount of ammonium heptamolybdate slowly to the slurry. Water was evaporated whilst stirring at 80 °C. The resulting solid was further dried in an oven and calcined at 550 °C for 6 h with a heating rate of 2 °C/min. The molybdenum-supported catalysts are denoted as Mo(x)SAPO-34@ZSM-5, Mo(x)H^+[SAPO-34@ZSM-5], and Mo(x)H^+ZSM-5@SAPO-34, where x corresponds to wt% Mo loading [9].

3.2. Characterization of the Parent and Composite Structures

Morphological features of the Mo-loaded samples were investigated by scanning electron microscopy (SEM). Zeolite textural properties were determined by nitrogen porosimetry, carried out at 77 K using an Autosorb-1 (Quantachrome, Boynton Beach, FL, USA) porosimeter. The samples were outgassed for at least 24 h at 350 °C and high vacuum (10^{-7} mbar). The specific total surface areas of the prepared samples were calculated using the BET equation and pore size distribution. The NLDFT method was applied to extract the pore size distribution. Finally the Mo content in all conformations after wet impregnation was estimated by electron microscope with an energy-dispersive X-ray spectrometer (SEM-EDS) (Oxford Instruments, Abingdon, UK). Calcination of SAPO-34, ZSM-5, and their corresponding core–shell structures was carried out at 550 °C for 12 h under flowing air. Thermogravimetric analysis (TGA) was performed on each sample in the temperature range of 30–700 °C. The amount of coke was obtained from the total weight loss. The effect of H^+ZSM-5 proportion as well as of metal loading on the acidity of composite ze-

olitic catalytic materials was investigated by means of the NH_3 temperature-programmed desorption method.

3.3. Performance of the Bifunctional Hierarchical Zeolite

The catalytic test rig developed in this work can accommodate both powdered samples (up to 3 g) and cylindrical monoliths (1 cm diameter, 7 cm length). The gas mixture—allowing the simultaneous introduction of two gases—can be preheated upstream of the reactor cell to temperatures of up to 500 °C (depending on the flow rate). Preheating is achieved using a series of wall-heated tubes (maximum wall temperature 850 °C) packed with 1 mm stainless-steel spheres. The reactor cell itself is electrically heated by an external heating jacket to temperatures as high as 800 °C. All pipelines from the preheaters to the reactor and from the reactor to the GC sampling valve are insulated with high-temperature materials wrapped in stainless-steel foil.

Two electronic mass flow controllers, operating in the ranges of 40–2000 mL min^{-1} and 4–200 mL min^{-1}, deliver the gas mixture to the reactor at constant flow. The analytical system (SRI GC) is equipped with a PID detector, offering high sensitivity and selectivity toward aromatics. The PID detector is positioned downstream of a TCD detector, and argon is used as the carrier gas. This configuration enables detection of the produced H_2 and aromatics, as well as analysis of the permanent gases fed to the reactor (methane, nitrogen, carbon dioxide) and intermediates formed during reaction (e.g., ethylene).

A 10-port gas sampling valve integrated with two columns—a fused-silica capillary molecular-sieve column and a stainless-steel capillary column for aromatic separation—using a reverse-flow technique allows complete separation of H_2, N_2, CH_4, CO, CO_2, ethylene, and aromatics in a single run (benzene elutes at 8.3 min). The system is additionally equipped with a liquid mass-flow controller (10–200 mg h^{-1}) and a bypass line for the reactor cell, enabling accurate PID calibration with various aromatic species.

For catalytic testing, the powdered sample (1.1 g) was loaded into the reactor cell, flushed with nitrogen, and maintained under nitrogen flow for 24 h at 500 °C. The temperature was then raised to 750 °C with the nitrogen flow set at 66.3 mL min^{-1}. After 2 h on stream, methane was introduced upstream of the reactor at 17.6 mL min^{-1}, and the first chromatographic run was recorded 13.5 min after initiating methane flow. This methane flow corresponds to an hourly space velocity of 77 h^{-1} (or 1 L h^{-1} g_cat^{-1}), with a methane concentration of 21 vol% in the CH_4/N_2 mixture.

4. Conclusions

This study demonstrates the critical impact of core–shell architecture, acidity modulation, and molybdenum dispersion on the catalytic performance of SAPO-34/ZSM-5 composites in the methane dehydroaromatization (MDA) reaction. In non-protonated SAPO-34@ZSM-5 composites, the low acidity of the Na-ZSM-5 shell limits both the dispersion and activation of Mo species. As a result, Mo predominantly remains as dispersed MoO_3, primarily located on the external surface or within the ZSM-5 micropores, leading to poor methane conversion and low benzene yield, irrespective of Mo loading.

Post-synthesis protonation of SAPO-34@ZSM-5 enhances both methane conversion and benzene selectivity, highlighting the pivotal role of acidic sites in promoting Mo dispersion and activation. Among the tested configurations, H^+ZSM-5@SAPO-34, particularly at a 3:1 mass ratio, proved to be the most effective composite. The higher proportion of H^+ZSM-5 in the core provides a greater density of strong acid sites, facilitating improved Mo anchoring and dispersion, which in turn promotes methane activation and efficient ethylene-to-benzene conversion. The synergistic integration of MFI and CHA topologies at

optimal ratios also creates a finely interconnected pore network, enhancing mass transport and accessibility to active sites.

In contrast, when the SAPO-34 content dominates, as in Mo(3)_H^+ZSM-5@SAPO-34[1], benzene yield decreases markedly, consistent with surface area and porosity analyses. This indicates that excessive SAPO-34 can impede Mo distribution and restrict access to active sites, underscoring the importance of balancing compositional ratios in core–shell designs.

In conclusion, these findings emphasize that precise engineering of zeolite acidity and pore structure is essential for developing efficient and durable MDA catalysts. Protonated, ZSM-5-rich composites, particularly at optimized SAPO-to-ZSM-5 ratios, demonstrate strong potential as next-generation catalysts for methane valorization.

Supplementary Materials: The following supporting information can be downloaded at https://www.mdpi.com/article/10.3390/catal16020161/s1. Figure S1: SAPO-34@ZSM-5 SEM images and XRD patterns of SAPO-34@ZSM-5 (a) before and (b) after calcination respectively. Figure S2: SEM images and XRD pattern of MoO_3-loaded SAPO-34. Table S1: Benzene selectivity values of SAPO-34@ZSM-5 and H^+ZSM-5@SAPO-34. Table S2: Theoritical prediction of composites specific surface area.

Author Contributions: Conceptualization, G.E.R. and F.K.K.; methodology, C.M.V.; validation, C.M.V., A.P. and G.E.R.; formal analysis, A.P., G.V.T. and G.E.R.; investigation, C.M.V.; resources, G.E.R. and F.K.K.; data curation, G.E.R.; writing—original draft preparation, C.M.V.; writing—review and editing, G.E.R. and F.K.K.; visualization G.E.R., C.M.V. and A.P.; supervision, G.E.R. and F.K.K.; project administration, G.E.R. and F.K.K.; funding acquisition, G.E.R. and F.K.K. All authors have read and agreed to the published version of the manuscript.

Funding: This research was funded by the European Union's Horizon 2020 research and innovation program (ZEOCAT-3D) under grant agreement No 814548.

Data Availability Statement: Data available on request from the authors.

Conflicts of Interest: The authors declare no conflicts of interest.

References

1. Guo, X.; Fang, G.; Li, G.; Ma, H.; Fan, H.; Yu, L.; Ma, C.; Wu, X.; Deng, D.; Wei, M.; et al. Direct, Nonoxidative Conversion of Methane to Ethylene, Aromatics, and Hydrogen. *Science* **2014**, *344*, 616–619. [CrossRef]
2. Kosinov, N.; Hensen, E.J.M. Reactivity, Selectivity, and Stability of Zeolite-Based Catalysts for Methane Dehydroaromatization. *Adv. Mater.* **2020**, *32*, 2002565. [CrossRef]
3. Matus, E.V.; Ismagilov, I.Z.; Sukhova, O.B.; Zaikovskii, V.I.; Tsikoza, L.T.; Ismagilov, Z.R.; Moulijn, J.A. Study of Methane Dehydroaromatization on Impregnated Mo/ZSM-5 Catalysts and Characterization of Nanostructured Molybdenum Phases and Carbonaceous Deposits. *Ind. Eng. Chem. Res.* **2007**, *46*, 4063–4074. [CrossRef]
4. Xu, Y.; Bao, X.; Lin, L. Direct conversion of methane under nonoxidative conditions. *J. Catal.* **2003**, *216*, 386–395. [CrossRef]
5. Tessonnier, J.-P.; Louis, B.; Rigolet, S.; Ledoux, M.J.; Pham-Huu, C. Methane dehydro-aromatization on Mo/ZSM-5: About the hidden role of Brønsted acid sites. *Appl. Catal. A Gen.* **2008**, *336*, 79–88. [CrossRef]
6. Tempelman, C.H.L.; Hensen, E.J.M. On the deactivation of Mo/HZSM-5 in the methane dehydroaromatization reaction. *Appl. Catal. B Environ.* **2015**, *176–177*, 731–739. [CrossRef]
7. Li, B.; Li, S.; Li, N.; Chen, H.; Zhang, W.; Bao, X.; Lin, B. Structure and acidity of Mo/ZSM-5 synthesized by solid state reaction for methane dehydrogenation and aromatization. *Microporous Mesoporous Mater.* **2006**, *88*, 244–253. [CrossRef]
8. Liu, H.; Shen, W.; Bao, X.; Xu, Y. Methane dehydroaromatization over Mo/HZSM-5 catalysts: The reactivity of MoCx species formed from MoO_x associated and non-associated with Brönsted acid sites. *Appl. Catal. A Gen.* **2005**, *295*, 79–88. [CrossRef]
9. Vollmer, I.; Mondal, A.; Yarulina, I.; Abou-Hamad, E.; Kapteijn, F.; Gascon, J. Quantifying the impact of dispersion, acidity and porosity of Mo/HZSM-5 on the performance in methane dehydroaromatization. *Appl. Catal. A Gen.* **2019**, *574*, 144–150. [CrossRef]
10. Kosinov, N.; Coumans, F.J.A.G.; Li, G.; Uslamin, E.; Mezari, B.; Wijpkema, A.S.G.; Pidko, E.A.; Hensen, E.J.M. Stable Mo/HZSM-5 methane dehydroaromatization catalysts optimized for high-temperature calcination-regeneration. *J. Catal.* **2017**, *346*, 125–133. [CrossRef]

11. Wilson, S.; Barger, P. The characteristics of SAPO-34 which influence the conversion of methanol to light olefins. *Microporous Mesoporous Mater.* **1999**, *29*, 117–126. [CrossRef]
12. Chen, J.; Thomas, J.M. Synthesis of SAPO-41 and SAPO-44 and their performance as acidic catalysts in the conversion of methanol to hydrocarbons. *Catal. Lett.* **1991**, *11*, 199–207. [CrossRef]
13. Agote-Arán, M.; Kroner, A.B.; Wragg, D.S.; Sławiński, W.A.; Briceno, M.; Islam, H.U.; Sazanovich, I.V.; Rivas, M.E.; Smith, A.W.J.; Collier, P.; et al. Understanding the Deactivation Phenomena of Small-Pore Mo/H-SSZ-13 during Methane Dehydroaromatisation. *Molecules* **2020**, *25*, 5048. [CrossRef]
14. Das, S.; Pérez-Ramírez, J.; Gong, J.; Dewangan, N.; Hidajat, K.; Gates, B.C.; Kawi, S. Core–shell structured catalysts for thermocatalytic, photocatalytic, and electrocatalytic conversion of CO_2. *Chem. Soc. Rev.* **2020**, *49*, 2937–3004. [CrossRef]
15. Wei, Y.; Feng, J.; Guan, B.; Yu, J. Structural Engineering of Hierarchical Zeolite-Based Catalysts. *Acc. Mater. Res.* **2024**, *5*, 857–871. [CrossRef]
16. Razavian, M.; Fatemi, S. Synthesis and application of ZSM-5/SAPO-34 and SAPO-34/ZSM-5 composite systems for propylene yield enhancement in propane dehydrogenation process. *Microporous Mesoporous Mater.* **2015**, *201*, 176–189. [CrossRef]
17. Li, X.; Rezaei, F.; Ludlow, D.K.; Rownaghi, A.A. Synthesis of SAPO-34@ZSM-5 and SAPO-34@Silicalite-1 Core–Shell Zeolite Composites for Ethanol Dehydration. *Ind. Eng. Chem. Res.* **2018**, *57*, 1446–1453. [CrossRef]
18. Wu, H.; Wang, X.; Liu, F.; Cao, J. Facile in situ hydrothermal crystallization synthesis of SAPO-34/ZSM-5 composite catalyst for methanol to olefin reaction. *J. Porous Mater.* **2019**, *26*, 793–802. [CrossRef]
19. Moradiyan, E.; Halladj, R.; Askari, S. Beneficial Use of Ultrasound in Rapid-Synthesis of SAPO34/ZSM-5 Nanocomposite and Its Catalytic Performances on MTO Reaction. *Ind. Eng. Chem. Res.* **2018**, *57*, 1871–1882. [CrossRef]
20. Chae, H.-J.; Song, Y.-H.; Jeong, K.-E.; Kim, C.-U.; Jeong, S.-Y. Physicochemical characteristics of ZSM-5/SAPO-34 composite catalyst for MTO reaction. *J. Phys. Chem. Solids* **2010**, *71*, 600–603. [CrossRef]
21. Liu, F.; Wang, X.; Xu, F.; Lin, Q.; Pan, H.; Wu, H.; Cao, J. Fabrication and characterization of composites comprising (CHA)SAPO-34 with (MFI)ZSM-5 topologies and their catalytic performances on MTO reaction. *Microporous Mesoporous Mater.* **2017**, *252*, 197–206. [CrossRef]
22. Chen, X.; Jiang, R.; Hou, H.; Zhou, Z.; Wang, X. Synthesis of ZSM-5/SAPO-34 zeolite composites from LAPONITE® and their catalytic properties in the MTO reaction. *CrystEngComm* **2020**, *22*, 6182–6188. [CrossRef]
23. Wu, H.; Liu, F.; Yi, Y.; Cao, J. Catalytic and deactivated behavior of SAPO-34/ZSM-5 composite molecular sieve synthesized by in-situ two-step method. *J. Mater. Res. Technol.* **2021**, *15*, 1844–1853. [CrossRef]
24. Jin, W.; Ma, J.; Ma, H.; Li, X.; Wang, Y. Hydrothermal synthesis of core-shell ZSM-5/SAPO-34 composite zeolites and catalytic performance in methanol-to-aromatics reaction. *J. Solid State Chem.* **2018**, *267*, 6–12. [CrossRef]
25. Zhang, L.; Jiang, Z.-X.; Yu, Y.; Sun, C.-S.; Wang, Y.-J.; Wang, H.-Y. Synthesis of core–shell ZSM-5@meso-SAPO-34 composite and its application in methanol to aromatics. *RSC Adv.* **2015**, *5*, 55825–55831. [CrossRef]
26. Jin, Z.; Liu, S.; Qin, L.; Liu, Z.; Wang, Y.; Xie, Z.; Wang, X. Methane dehydroaromatization by Mo-supported MFI-type zeolite with core–shell structure. *Appl. Catal. A Gen.* **2013**, *453*, 295–301. [CrossRef]
27. Hong, D.-Y.; Kim, H.S.; Zhang, H.; Kang, S.K.; Tikue, E.T.; Lee, P.S. Si–OH Nest and Al Distribution of Silicalite-1 Core/Al-ZSM-5 Shell Zeolites for Methane Dehydroaromatization Reaction. *Crystals* **2021**, *11*, 647. [CrossRef]
28. Qiao, Y.; Yang, M.; Gao, B.; Wang, L.; Tian, P.; Xu, S.; Liu, Z. Creation of hollow SAPO-34 single crystals via alkaline or acid etching. *Chem. Commun.* **2016**, *52*, 5718–5721. [CrossRef]
29. Askari, S.; Halladj, R. Ultrasonic Pretreatment for Hydrothermal Synthesis of SAPO-34 Nanocrystals. *Ultrason. Sonochem.* **2012**, *19*, 554–559. [CrossRef]
30. Beuque, A.; Valtchev, V.; Mintova, S.; Gilson, J.-P.; Pinard, L. Identification of reversible and irreversible deactivation of MDA catalysts: A key to design a viable process. *J. Catal.* **2023**, *426*, 39–51. [CrossRef]
31. Sun, Q.; Ma, Y.; Wang, N.; Li, X.; Xi, D.; Xu, J.; Deng, F.; Yoon, K.B.; Oleynikov, P.; Terasaki, O.; et al. High performance nanosheet-like silicoaluminophosphate molecular sieves: Synthesis, 3D EDT structural analysis and MTO catalytic studies. *J. Mater. Chem. A* **2014**, *2*, 17828–17839. [CrossRef]
32. Li, L.; Cui, X.; Li, J.; Wang, J. Synthesis of SAPO-34/ZSM-5 Composite and Its Catalytic Performance in the Conversion of Methanol to Hydrocarbonsc. *J. Braz. Chem. Soc.* **2015**, *26*, 290–296. [CrossRef]
33. Jain, R.; Mallette, A.J.; Rimer, J.D. Controlling Nucleation Pathways in Zeolite Crystallization: Seeding Conceptual Methodologies for Advanced Materials Design. *J. Am. Chem. Soc.* **2021**, *143*, 21446–21460. [CrossRef] [PubMed]
34. Valtchev, V.; Gilson, J.-P.; Rimer, J.D.; Steed, J.W. Zeolite Crystal Engineering. *Cryst. Growth Des.* **2023**, *23*, 7555–7557. [CrossRef]
35. Veziri, C.M.; Palomino, M.; Karanikolos, G.N.; Corma, A.; Kanellopoulos, N.K.; Tsapatsis, M. Toward Submicrometer c-Oriented Nanoporous Films with Unidimensional Pore Network: AFI Film Morphology Control by Precursor Mixture Manipulation. *Chem. Mater.* **2010**, *22*, 1492–1502. [CrossRef]
36. Chen, H.; Wang, M.; Yang, M.; Shang, W.; Yang, C.; Liu, B.; Hao, Q.; Zhang, J.; Ma, X. Organosilane surfactant-directed synthesis of nanosheet-assembled SAPO-34 zeolites with improved MTO catalytic performance. *J. Mater. Sci.* **2019**, *54*, 8202–8215. [CrossRef]

37. Wang, D.; Zhang, L.; Li, J.; Kamasamudram, K.; Epling, W.S. NH_3-SCR over Cu/SAPO-34–Zeolite acidity and Cu structure changes as a function of Cu loading. *Catal. Today* **2014**, *231*, 64–74. [CrossRef]
38. Zandonai, C.H.; Yassue-Cordeiro, P.H.; Castellã-Pergher, S.B.; Scaliante, M.H.N.O.; Fernandes-Machado, N.R.C. Production of petroleum-like synthetic fuel by hydrocracking of crude soybean oil over ZSM5 zeolite–Improvement of catalyst lifetime by ion exchange. *Fuel* **2016**, *172*, 228–237. [CrossRef]
39. Stepanov, A.A.; Korobitsyna, L.L.; Vosmerikov, A.V. Investigation of the Properties of Mo/ZSM-5 Catalysts Based on Zeolites with Microporous and Micro–Mesoporous Structures. *Chemistry* **2023**, *5*, 1256–1270. [CrossRef]
40. López-Martín, A.; Caballero, A.; Colón, G. Structural and surface considerations on Mo/ZSM-5 systems for methane dehydroaromatization reaction. *Mol. Catal.* **2020**, *486*, 110787. [CrossRef]
41. Mannei, E.; Ayari, F.; Asedegbega-Nieto, E.; Mhamdi, M.; Delahay, G. Catalytic behaviour of molybdenum-based zeolitic materials prepared by organic-medium impregnation and sublimation methods. *J. Iran. Chem. Soc.* **2020**, *17*, 1087–1101. [CrossRef]
42. Rodríguez-González, L.; Hermes, F.; Bertmer, M.; Rodríguez-Castellón, E.; Jiménez-López, A.; Simon, U. The acid properties of H-ZSM-5 as studied by NH_3-TPD and 27Al-MAS-NMR spectroscopy. *Appl. Catal. A Gen.* **2007**, *328*, 174–182. [CrossRef]
43. Zachariou, A.; Hawkins, A.P.; Howe, R.F.; Skakle, J.M.S.; Barrow, N.; Collier, P.; Nye, D.W.; Smith, R.I.; Stenning, G.B.G.; Parker, S.F.; et al. Counting the Acid Sites in a Commercial ZSM-5 Zeolite Catalyst. *ACS Phys. Chem. Au* **2023**, *3*, 74–83. [CrossRef] [PubMed]
44. Zhao, K.; Jia, L.; Wang, J.; Hou, B.; Li, D. The influence of the Si/Al ratio of Mo/HZSM-5 on methane non-oxidative dehydroaromatization. *New J. Chem.* **2019**, *43*, 4130–4136. [CrossRef]
45. Duan, C.; Zhang, X.; Zhou, R.; Hua, Y.; Zhang, L.; Chen, J. Comparative studies of ethanol to propylene over HZSM-5/SAPO-34 catalysts prepared by hydrothermal synthesis and physical mixture. *Fuel Process. Technol.* **2013**, *108*, 31–40. [CrossRef]
46. Han, S.J.; Kim, S.K.; Hwang, A.; Kim, S.; Hong, D.-Y.; Kwak, G.; Jun, K.-W.; Kim, Y.T. Non-oxidative dehydroaromatization of methane over Mo/H-ZSM-5 catalysts: A detailed analysis of the reaction-regeneration cycle. *Appl. Catal. B Environ.* **2019**, *241*, 305–318. [CrossRef]
47. Liu, S.; Wang, L.; Ohnishi, R.; Ichikawa, M. Bifunctional Catalysis of Mo/HZSM-5 in the Dehydroaromatization of Methane to Benzene and Naphthalene XAFS/TG/DTA/MASS/FTIR Characterization and Supporting Effects. *J. Catal.* **1999**, *181*, 175–188. [CrossRef]
48. Kosinov, N.; Coumans, F.J.A.G.; Uslamin, E.A.; Wijpkema, A.S.G.; Mezari, B.; Hensen, E.J.M. Methane Dehydroaromatization by Mo/HZSM-5: Mono- or Bifunctional Catalysis? *ACS Catal.* **2017**, *7*, 520–529. [CrossRef]
49. Li, G. Methane dehydroaromatization catalyzed by Mo/ZSM-5: Location-steered activity and mechanism. *Chem. Commun.* **2023**, *59*, 10932–10935. [CrossRef]
50. Vollmer, I.; Abou-Hamad, E.; Gascon, J.; Kapteijn, F. Aromatization of Ethylene–Main Intermediate for MDA? *ChemCatChem* **2020**, *12*, 544–549. [CrossRef]
51. Borry, R.W.; Kim, Y.H.; Huffsmith, A.; Reimer, J.A.; Iglesia, E. Structure and Density of Mo and Acid Sites in Mo-Exchanged H-ZSM5 Catalysts for Nonoxidative Methane Conversion. *J. Phys. Chem. B* **1999**, *103*, 5787–5796. [CrossRef]
52. Kosinov, N.; Uslamin, E.A.; Coumans, F.J.A.G.; Wijpkema, A.S.G.; Rohling, R.Y.; Hensen, E.J.M. Structure and Evolution of Confined Carbon Species during Methane Dehydroaromatization over Mo/ZSM-5. *ACS Catal.* **2018**, *8*, 8459–8467. [CrossRef] [PubMed]